



## RESEARCH ARTICLE

10.1029/2022JD038467

### Key Points:

- Unique observations show atmospheric gravity waves (AGWs) recurred along the South China Sea (SCS) for 4 days, exhibiting a pronounced periodicity of about 18 hr
- The Weather Research and Forecasting model was implemented to show that the AGWs are unique upstream waves generated by the interaction of wind and topography
- Recurring AGWs are rare, only happening when persistent air masses confront over the SCS, causing a small atmosphere-sea temperature bias

### Correspondence to:

X. Li,  
lix@qdio.ac.cn

### Citation:

Liu, A., Shen, D., & Li, X. (2023). Satellite observations and a numerical study of recurring atmospheric gravity waves along the South China Sea coast. *Journal of Geophysical Research: Atmospheres*, 128, e2022JD038467. <https://doi.org/10.1029/2022JD038467>

Received 1 JAN 2023

Accepted 1 AUG 2023

## Satellite Observations and a Numerical Study of Recurring Atmospheric Gravity Waves Along the South China Sea Coast

Aiyue Liu<sup>1,2</sup>, Dongliang Shen<sup>1</sup> , and Xiaofeng Li<sup>1</sup> 

<sup>1</sup>Key Laboratory of Ocean Circulation and Waves, Institute of Oceanology, Chinese Academy of Sciences, Qingdao, China,

<sup>2</sup>University of Chinese Academy of Sciences, Beijing, China

**Abstract** Several groups of diurnal recurring atmospheric gravity waves (AGWs) were observed on an Environmental Satellite advanced synthetic aperture radar image and six Moderate Resolution Imaging Spectroradiometer (MODIS) images acquired along the South China Sea coast for 4 days from 3 to 6 March 2010. The unique observations are that the previously observed AGWs seldom recurred in a region for multiple days. Each cycle of these observed AGWs had undergone three stages: generation, propagation, and dissipation daily. Both SAR-imaged sea surface roughness patterns and MODIS-observed cloud imprints show that the AGWs were a group of transverse waves along the coast. We implemented the Weather Research and Forecasting (WRF) model to understand the physical characteristics and dynamical mechanisms of these AGWs. The WRF simulated results indicated that the AGWs were upstream waves triggered by the interaction of the southerly wind and topography and dissipated by the diurnal warming. We applied the spectral analysis to the model-simulated vertical wind field and explored that the leading wave crest length and crest-to-crest wavelength are 156.25 and 7.14 km, respectively. The wave period and phase speed of the upstream AGWs within the vital observation of SAR are 1.81 hr and 1.26 m/s, respectively. The fifth-generation European Centre for Medium-Range Weather Forecasts reanalysis hourly data was used to explore the rarity of the recurring AGWs and proved that the stable air-sea temperature difference was the main reason for the rarity of this event. And sufficient cloud content (>50%) was necessary for the MODIS to capture the AGWs' imprints.

**Plain Language Summary** Satellite observations show that the atmospheric gravity waves generated, propagated, and dissipated along the South China Sea coast daily for four consecutive days, which were never consistently captured before. We implemented the Weather Research and Forecasting model to simulate the entire processes of the atmospheric gravity waves (AGWs). Southerly winds, with an average strength of 10 m/s, blew over the region but were blocked by the Yunkai Mountain near the coast. This obstruction induced a dynamic atmospheric disturbance, resulting in the generation of upstream gravity waves late at night. Subsequently, these gravity waves underwent a reinforcement stage until early morning the next day and continued propagating offshore from early morning until high noon. After that, the AGWs started decaying and finally disappeared at about 08:30 UTC (16:30 local time). The evolution of these AGWs had a remarkable 18-hr period during these regular processes. Moreover, this unique process was caused by the persistent balance of cold and warm air masses.

## 1. Introduction

Atmospheric gravity waves (AGWs), a critical atmospheric fluctuating process, are internal waves for which gravity is the restoring force in the atmosphere (Francis, 1975; Nappo, 2013). The possible generation mechanisms include the wind oscillations induced by a mountain (Li et al., 2011; Zheng et al., 1998), vertical air transport near a cold front (Eckermann & Vincent, 1993; Koch et al., 2005), vertical convection near a tropical storm center (Kuester et al., 2008; Xu et al., 2016), and land-sea breeze interaction in the coastal region (Du et al., 2019). AGWs can propagate either upstream or downstream depending upon the Froude number (Baines, 1998; Ertekin et al., 1990), topographic forcing (Baines, 1977), and stratification in the marine atmospheric boundary layer (MABL) (Vachon et al., 1994). Scorer number is mainly employed to assess the suitability of the environment for horizontal wave propagation, thereby determining the extent to which waves can influence a larger geographical area. In addition, the varying background winds and atmospheric conditions (temperature, humidity, density, etc.) affect AGWs' propagation and dissipation processes (C. O. Hines & Reddy, 1967). The propagation of AGWs can also modulate wind, moisture, and temperature (Chunchuzov et al., 2000), transfer

© 2023. The Authors.

This is an open access article under the terms of the [Creative Commons Attribution License](#), which permits use, distribution and reproduction in any medium, provided the original work is properly cited.

the momentum and kinetic energy from the lower to the upper atmosphere, and cause air turbulences when they break. Therefore, it is vital to observe and analyze AGWs accurately.

Observation of the AGWs is relatively common in satellite remote-sensing images. The wind associated with AGWs modulates sea surface roughness at the bottom of MABL, and changes values in the synthetic aperture radar (SAR) normalized radar cross section (NRCS) through the Bragg resonant-scattering mechanism (Valenzuela, 1978). As a result, AGWs appear as bright-and-dark patterns on active remote sensing (SAR) images. Since AGWs also modulate the atmospheric temperature, humidity, and cloud structure, they can be imaged by passive visible and infrared remote-sensing sensors like Moderate Resolution Imaging Spectroradiometer (MODIS) onboard the National Aeronautics and Space Administration (NASA) Terra and Aqua satellites. However, under areas covered by high-level cloud or cloud-free conditions, MODIS can not always detect AGWs, even if it exists (Astafurov & Skorokhodov, 2017; Evdoshenko, 2016). Therefore, a combination of active (SAR) and passive (MODIS) remote sensing technology is ideal for observing AGWs (Gan et al., 2008; Li et al., 2002). From satellite images, AGW parameters such as wavelength, amplitude, and propagation directions can be measured directly (Qing et al., 2008). However, the vertical variation, lifelong evolution, and generation mechanisms cannot be derived from these satellite snapshots. As a result, implementing numerical atmospheric models (Mesinger & Arakawa, 1976) is an efficient and common method for studying AGWs' spatiotemporal characteristics.

In satellite observational studies, the life cycle of AGWs usually occurs within a day and does not recur for several days in a roll. The reason is that the thermodynamic and dynamic conditions change rapidly. As a result, AGW differs greatly from its oceanic counterpart, the oceanic internal wave. IWs are periodically generated in the global oceans by semi-diurnal tides daily because the environment (stratification, temperature, salinity, etc.) does not vary abruptly over a few days (Da Silva et al., 1998; Zhang et al., 2020).

This paper acquired a series of SAR and MODIS images which subsequently proved that they contained the imprint of AGWs in the east of the Leizhou Peninsula in the northern South China Sea (SCS). This article aims to comprehensively understand the recurring-AGWs' generation mechanisms and the dynamical processes. This paper is organized as follows: satellite observations are described in Section 2. Next, Section 3 describes the numerical model setup, validation, and analysis of simulation results. Then, in Section 4, we based on the model results and reanalysis data to explore the dynamic process and characteristic specificity of these AGWs. The conclusions are finally presented in Section 5.

## 2. Satellite Observations

The study area is northern SCS, as shown in Figure 1. Hainan Island and the Leizhou Peninsula constitute a special semi-enclosed terrain in the coastal area of the northern SCS. The Leizhou Peninsula has a typical tropical climate. In March, early spring, the Leizhou Peninsula experiences an average monthly temperature of 22°C and prevailing southwest winds. Yunkai Mountain, near the SCS, is shown in the red box in Figure 1b. It covers over 1,300 km<sup>2</sup> and peaks over 800 m above sea level. Figure 2a is a 150-m resolution ENVISAT advanced synthetic aperture radar (ASAR) VV image acquired at 02:33 UTC on 3 March 2010. The European Space Agency ENVISAT satellite was launched in 2002, carrying C-band SAR with horizontal-horizontal (HH) and vertical-vertical (VV) polarizations (Mouche et al., 2005). This SAR image is a wide swath image of 400 km. A group of five alternate brighter-darker lines parallel to the coastline in this SAR image is recognized as the atmospheric wave packet with a wavelength between 5 and 10 km. The bright line delineates the region characterized by high wind speeds, whereas the dark line corresponds to the region with low wind speeds. SAR presents the detailed sea surface roughness patterns and measures the physical parameter NRCS that can be used to derive sea surface winds using the family of C-band geophysical model functions (Hersbach, 2010; Stoffelen et al., 2017). This study uses the CMOD5N geophysical model function (Verhoef et al., 2008) to derive the wind speed at 10 m above the sea surface to validate the Weather Research and Forecasting Model (WRF) results. The inputs of the CMOD5N algorithm include the 10 m height wind direction from the fifth generation European Centre for Medium-Range Weather Forecasts reanalysis data (ERA5) and NRCS derived from the SAR image. Figure 2b shows that the SAR wind speed is ~2–12 m/s within the wavelike area (red box in Figure 2b).

MODIS provides high radiometric resolution image data for all surfaces with sunlight reflection and thermal radiation, creating conditions for observing cloud characterizations. The MODIS visible band images with 500-m

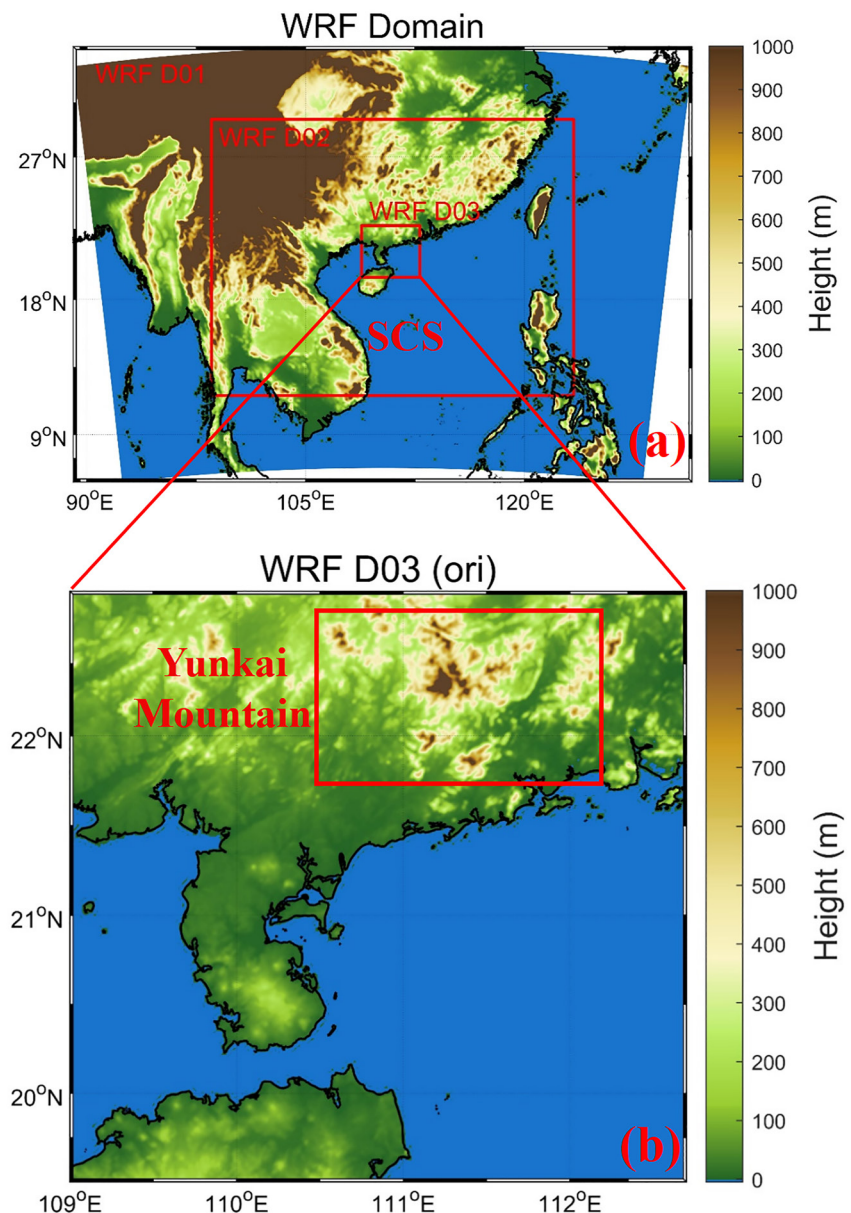


**Figure 1.** The Weather Research and Forecasting (WRF) model with the triple nested domains is shown in (a). WRF Domain-3 topographic map is shown in (b), and the red box marks Yunkai Mountain.

spatial resolution were used in this study to detect the AGWs-affected clouds further. A total of six MODIS images covering the study area between 3 and 6 March 2010, are depicted in Figure 3. Figures 3a and 3b present the same AGW at 03:50 and 05:25 UTC on 3 March, which indicates that during this period, AGW propagated 6.71 km to the offshore region with a phase speed of  $\sim 1.20$  m/s. On 4 March (Figures 3c and 3d), similar to the results on 3 March, the AGW propagated 8.85 km southward with a wave speed of  $\sim 1.90$  m/s from 02:55 to 06:05 UTC. Thus, MODIS observations suggest that these atmospheric waves are upstream AGWs. It can be seen that the AGWs are evident in the coastal ocean region. The crest-to-crest distance of the wave train in the MODIS image matches the SAR measurement.

The six MODIS images captured similar cloud characteristics at the same location. Moreover, these six consecutive MODIS images, taken over four consecutive days, indicate that this atmospheric fluctuation was a multi-day continuous phenomenon. We analyzed historical MODIS data from 2000 to 2022 and found that the diurnally recurring AGWs only exist in this study case. There are two possibilities to continuously observe AGWs from

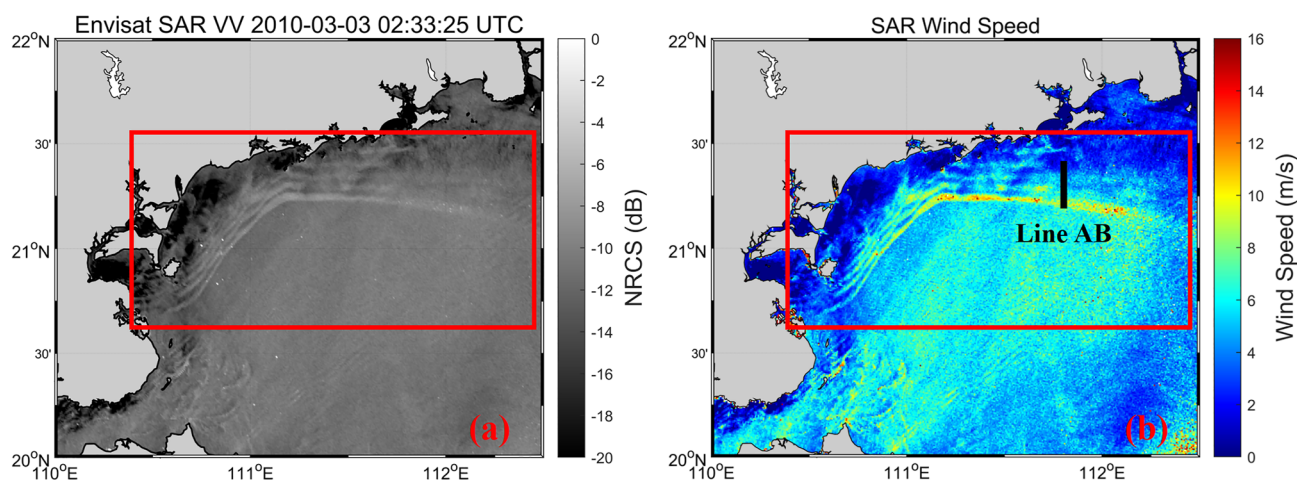


**Figure 2.** (a) Synthetic aperture radar (SAR) image observed at 02:33:25 UTC on 3 March 2010. (b) The wind speed at 10 m above the sea surface from the SAR image. The red boxes indicate the wavelike areas.

SAR and MODIS images in the same area. The first is that the same group of AGWs is produced and maintained for several days due to a suitable environment. The second is that there exists a daily periodic mechanism controlling AGWs' generation, propagation, and dissipation.

### 3. Materials and Methods

#### 3.1. Model Setup

To understand the generation mechanisms that induced these recurring AGWs, the WRF model, a numerical atmospheric model (Powers et al., 2017; Skamarock et al., 2019), was implemented to simulate AGWs on the east side of the Leizhou Peninsula. A triple nested domain with spatial resolutions of 9, 3, and 1 km is used in this simulation (Figure 1a). The outer domain (D01) spans from 6.0°N to 32.1°N and 92.7°E to 127.9°E. The middle nest domain (D02) is from 11.8°N to 28.5°N and 100.0°E to 121.7°E. The inner domain (D03) covers both sides of the Peninsula from 19.4°N to 22.7°N and 108.9°E to 113°E. There are 41 sigma levels in the vertical direction, with the model top at 100 hPa. The National Centers for Environmental Prediction (NCEP) Climate Forecast System Reanalysis (CFSR) data with 0.3-degree spatial resolution and 6-hourly temporal resolution initialized the WRF model and provided the lateral boundary conditions. The physical parameterizations in this simulation include WDM 6-class scheme (Hong et al., 2010; Lim & Hong, 2010), Kain-Fritsch Eta cumulus scheme (Kain, 2004), Monin-Obukhov surface-layer scheme (Jiménez et al., 2012), RRTMG longwave/shortwave radiation scheme (K. M. Hines et al., 2019), YSU planetary boundary layer (PBL) scheme (Hu et al., 2013), and Noah land-surface model (Ek et al., 2003; Skamarock et al., 2019). This scheme set has been proven excellent in simulating the dynamic and thermodynamic processes of MABL phenomena (Li et al., 2015, 2016; Xu et al., 2016). We performed the simulation from 00:00 UTC on 2 March to 00:00 UTC on 7 March 2010.

#### 3.2. Model-Simulated Wind Validation

At the SAR imaging time, the WRF-simulated sea surface wind map (Figure 4a red box) exhibits similar quasi-linear wave-like patterns as the SAR observation (Figure 2b red box). Line AB is perpendicular to the wave crests. We extracted SAR-derived wind data along Line AB. The corresponding WRF-simulated wind data were then interpolated to calculate the wind speed correlation between SAR and WRF. The result shows that SAR-derived and WRF-simulated wind speeds have the same oscillation scales in the horizontal and vertical directions (Figure 4b), with a correlation coefficient being 0.83. However, there is an understandable wind range difference between the two winds (Li et al., 2011). The average wind speeds of SAR and WRF are 6.27 and 5.16 m/s, respectively. Meanwhile, we used Cross Calibrated Multi-Platform (CCMP, <https://www.remss.com/measurements/ccmp/>) wind field data as an auxiliary verification. The mean absolute error (MAE) of the wind speed between the 2D CCMP and WRF wind speed at 10 m above the sea surface is 1.87 m/s. The high correlation of fluctuation scales and the low average wind speed MAE both indicate this simulation has credible results.

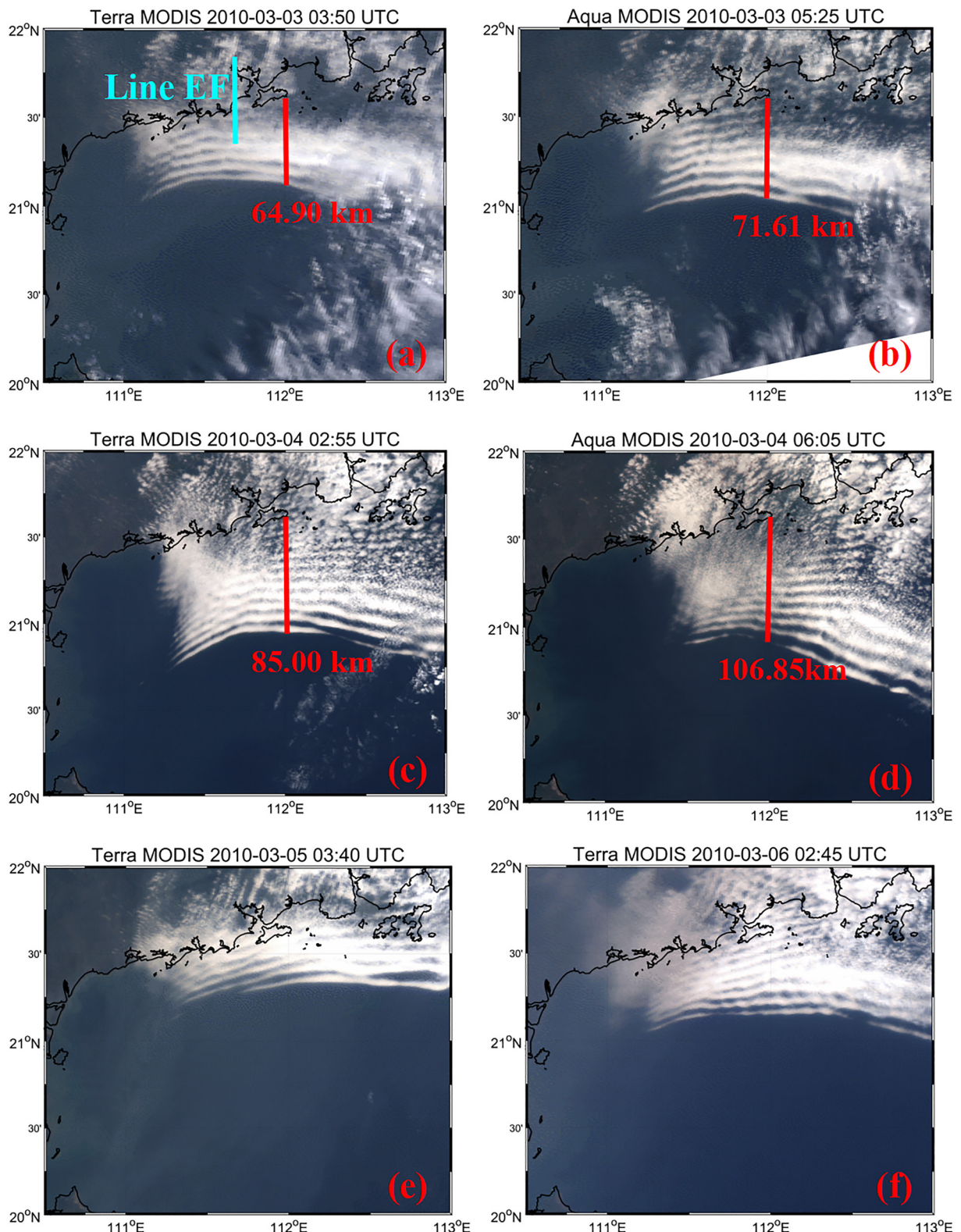


**Figure 3.** MODIS true color images at 03:50 and 05:25 UTC on 3 March (a and b), at 02:55 and 06:05 UTC on 4 March (c and d), at 03:40 UTC on 5 March (e), and at 02:45 UTC on 6 March (f).

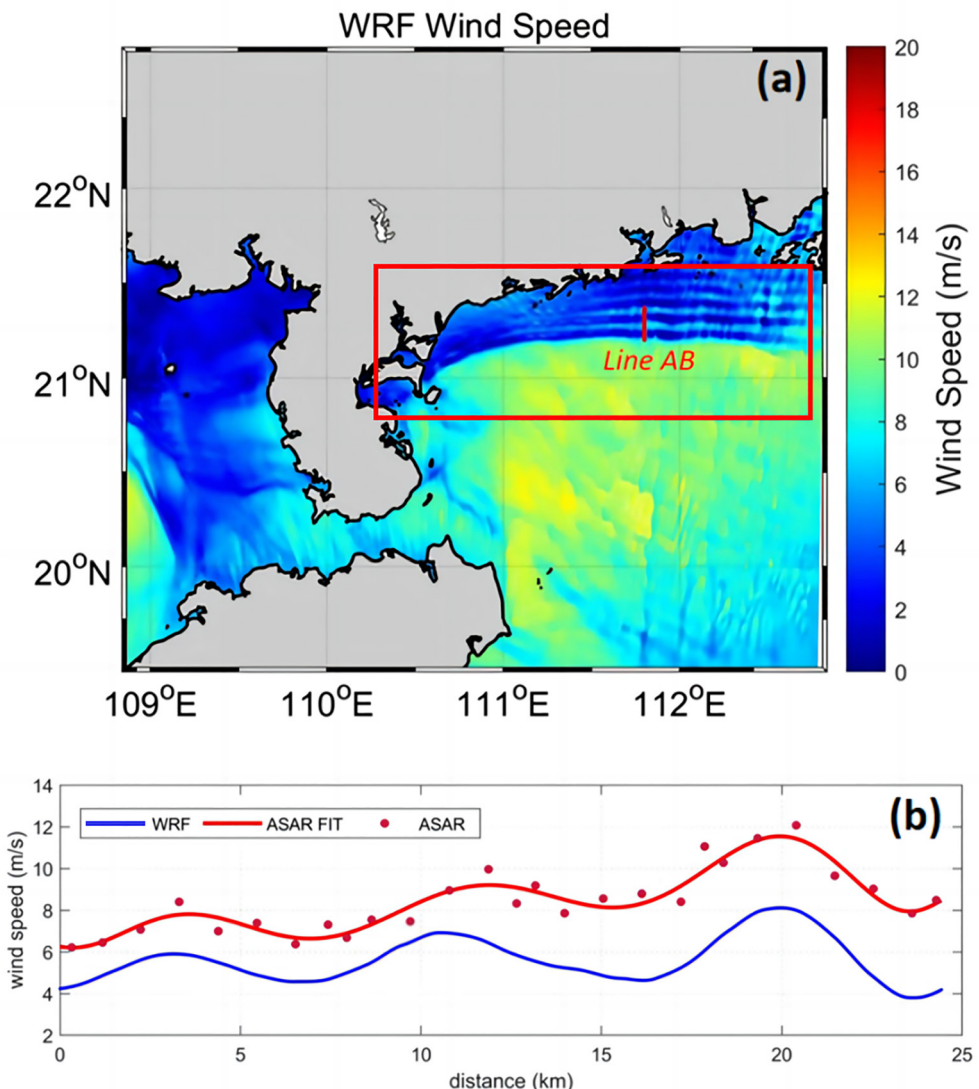


**Figure 4.** The wind speed at 10 m above the sea surface from the Weather Research and Forecasting (WRF) model is shown in (a), and the comparison of WRF simulated surface wind speed along Line AB with the independent synthetic aperture radar measurements is shown in (b).

### 3.3. Model Simulated AGW Physical Characteristics at the SAR Imaging Time

Figure 5 shows the WRF simulated fields at 950 hPa (~540 m height above the sea surface) at 02:30 UTC on 3 March, which is the most pronounced height of fluctuation at the SAR imaging time. The parameters include horizontal wind vectors, vertical wind velocity, relative humidity, potential temperature, cloud fraction, and PBL height. The southwesterly wind dominated the east side of the Leizhou Peninsula on 3 March. The horizontal wind speed shows a similar but stronger wave pattern at 950 hPa level (Figure 5a) than the SAR observation at the sea surface (Figure 2b) along the coastal region. The height difference caused a difference in the amplitude of the wind speed fluctuation, which indicated that the AGWs observed via satellite measurements within the atmosphere primarily comprise horizontally propagating waves confined to the atmospheric boundary layer. These waves exhibit less amount of energy propagating in the upward direction (Bretherton, 1969; Liu et al., 2010). Meanwhile, the wind speed gradually weakened from 15 to 12 m/s when the wind blew from the open ocean to the coastal region at 950 hPa. Figure 5b indicates that the largest fluctuation occurred in the region about 38 km offshore, and the max vertical wind speed was about 1.5 m/s.

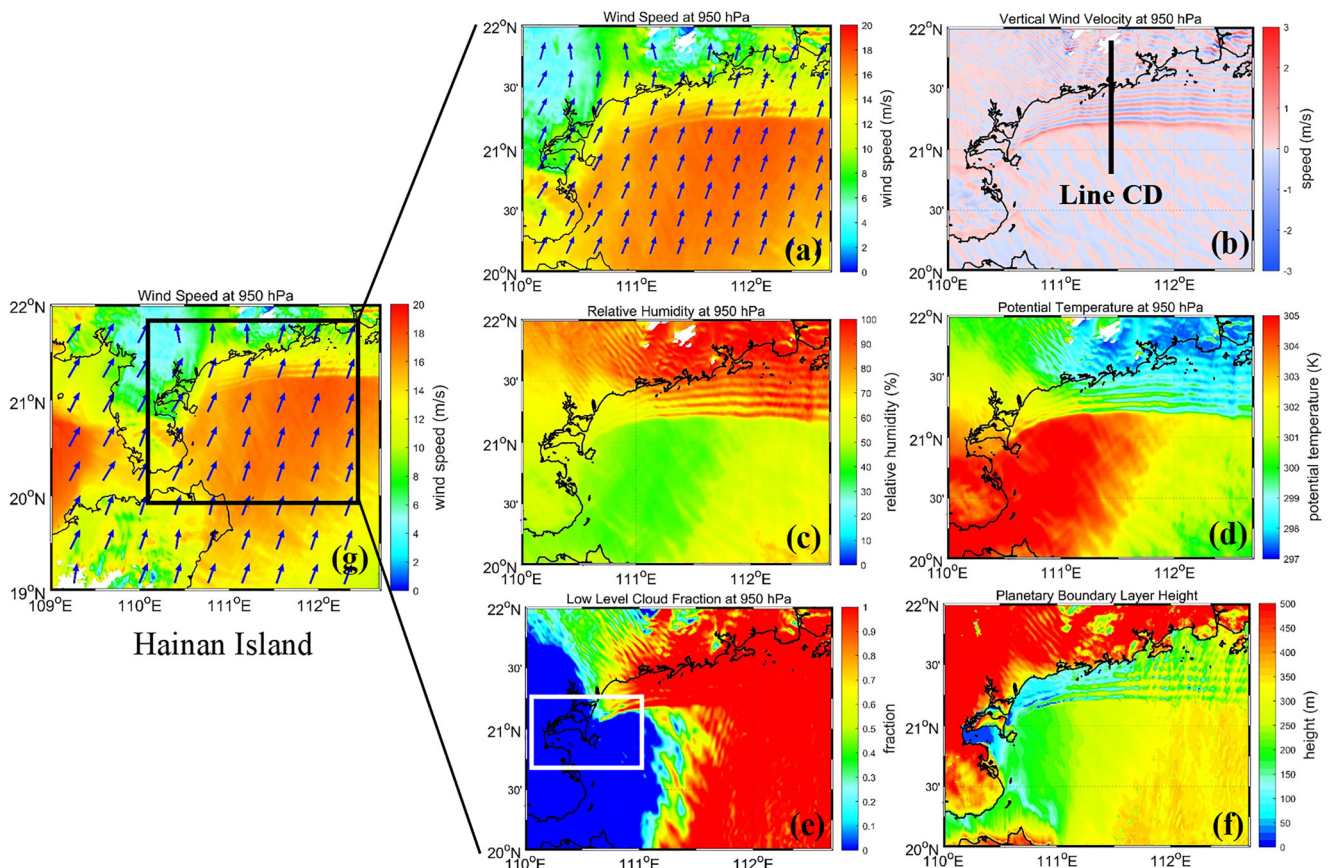


**Figure 5.** The Weather Research and Forecasting simulated horizontal wind speed with vectors (a), vertical wind velocity (b), relative humidity (c), potential temperature (d), low level could fraction (e) on the east side of the Leizhou Peninsula at 950 hPa at 02:30 UTC on 3 March 2010. (f) Shows the planetary boundary layer height at the corresponding time. (g) Represents a horizontal wind speed map with a larger area (including Hainan Island).

The relative humidity and potential temperature exhibit the thermodynamic characteristics of AGWs (Figures 5c and 5d). Figure 5c reveals the lower atmosphere on the left of the AGWs area (east coast of the Leizhou Peninsula) is drier. Adequate moisture or high relative humidity in the atmosphere is a prerequisite for cloud formation (Mendoza et al., 2021). Figure 5e shows that the cloud fraction content of the AGWs area was up to 90%, but it is very low (~10%) on the left of the AGWs area. The prevailing southwesterly wind (Figure 5a) during the study period suggested that the interaction between the wind and Hainan Island would impede the transportation of water vapor, resulting in a reduction in water vapor content to the left of the AGWs area (Figure 5g). Consequently, no clouds were present in that area (white box in Figure 5e). The wave pattern of potential temperature near the coast is opposite to the relative humidity. The high temperature implies that the air can hold more water to decrease relative humidity. Figure 5d shows that the potential temperature in the AGW's area is lower than that of the surrounding atmosphere and maintained at about 296–300 K. The main reason is the adiabatic effect associated with the gravity waves. The fluctuations in the vertical direction of AGWs compress the surrounding air mass, increasing the air pressure around it at the same altitude. The potential temperature decreases with the increase of air pressure. Thus, the relative humidity and potential temperature exhibit contrary fluctuations, as shown in Figures 5c and 5d.

The PBL height is also related to the AGWs, indicating changes in air buoyancy, local convection, and stability (Stull, 1988). The atmospheric fluctuation directly modulated the PBL height pattern, as shown in Figure 5f. The PBL height in the AGWs area also shows a wavelike pattern, with the lowest value being 150 m. When the AGWs oscillated downward, the boundary layer was compressed, decreasing the PBL layer height. The low PBL height made the AGWs sensitive to environmental changes in wind speed, sea surface temperature, and land-sea differential temperature (Ollier et al., 2018). Figures 5a–5f show similar fluctuating signals to the satellite observations, indicating simulation successfully captured surface field variations associated with this group of AGW.

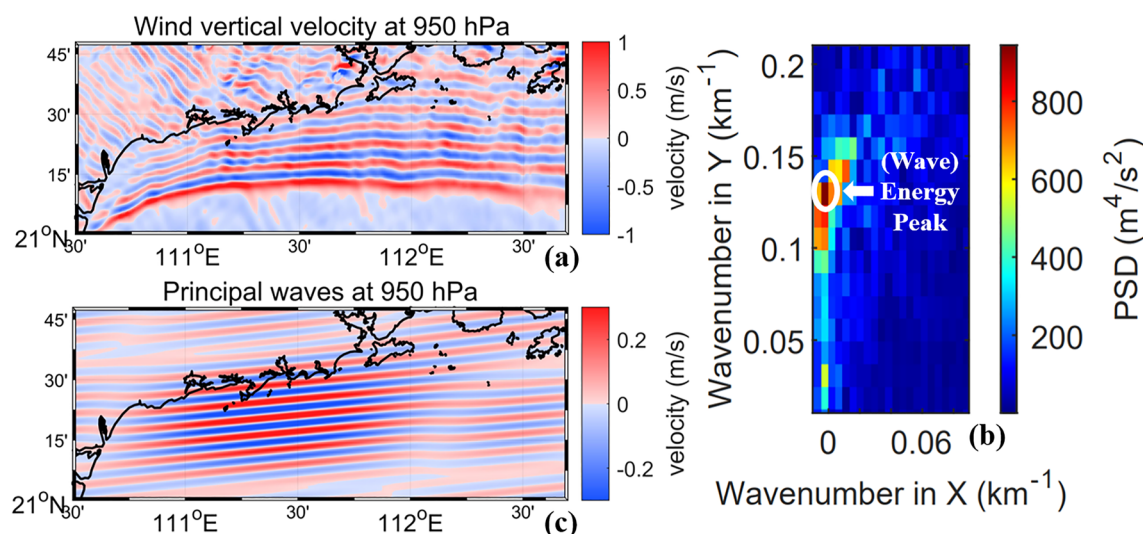


**Figure 6.** The 2D-spatial detrended wind vertical velocity (a) at 950 hPa at 02:30 UTC on 3 March 2010. (b) The 2D-spatial spectrum of (a). The white oval marks the peak of the spectrum. The vertical velocity in (c) is calculated based on the principal waves observed within the white oval in (b).

### 3.4. Model Simulated AGW Morphological Characteristics at the SAR Imaging Time

Two-dimensional Fast Fourier Transform (2D-FFT) was used to explore the morphological characteristic based on the detrended vertical velocity (Figure 6a) at 950 hPa at 02:30 UTC on 3 March 2010. The purpose of “detrended” is to remove the long-period fluctuating trends of the AGWs. The white oval of the 2D-spatial spectrum (Figure 6b) represented the waves with the strongest energy, namely, the principal wave pattern, which is shown in Figure 6c. The wavelength of the principal wave, perpendicular to the wave crests in Figure 6c, is 7.14 km. The length of the leading wave crest is 156.25 km. The wavelength of the principal wave was similar to the SAR observed wavelength, ranging from 5 to 10 km, which was significantly smaller than the wavelengths reported in previous studies along the China Sea coast. For example, Chunchuzov et al. (2000), reported topography-induced AGWs with wavelengths of 10–12 km, Gan et al. (2008), observed offshore jets-induced AGWs with wavelengths of 13–20 km, Li et al. (2011), found topography-induced AGWs with wavelengths of 12 km, and Li et al. (2016), studied extratropical Cyclone-induced AGWs with wavelengths of 20–30 km. These different studies highlight how various generation mechanisms can result in different wavelength scales of AGWs.

### 3.5. Time Series Analysis of the Daily Periodic Oscillation of Vertical Wind Velocity

To explore the temporal characteristic of the AGWs, we analyzed the time series of WRF-simulated vertical velocity along Line CD in Figure 5. The Line CD is perpendicular to the AGWs' crests and passes through the position of the strongest amplitude of the AGWs. The time series in Figure 7a runs from 14:30 UTC on 2 March to 14:30 UTC on 4 March, for a total of 48 hr covering the vital SAR observation. A daily scale recurring period of the AGWs, about 18 hr, was found in the model results. In each daily scale recurring period, three specific stages could be divided, including (a) generation/reinforcement stage, (b) offshore propagation stage, and (c) decay stage. For example, AGWs were generated and reinforced near the coast marked by the vertical black line in Figure 7a, indicating propagation's starting time around 14:30 UTC on 2 March. Whereafter, AGWs propagated offshore from 18:30 UTC on 2 March to 04:30 UTC on 3 March. In Figure 7a, the thin black arrows pointing left represent southerly winds blowing from the ocean toward the shoreline, and the crest line grows to the right with time, corresponding to the southward propagation of the waves. Consequently, AGWs both propagate against the wind to the south in the local daytime, which indicates that these waves are upstream AGWs. The average wind originated from truth south ( $\sim 360^\circ$ ) with a wind speed of 4 m/s near the coast on 2 March in the AGWs propagation stage. On 3 March, there was a southeasterly wind ( $\sim 300^\circ$ ) with an average wind speed of 8 m/s near the coast in the propagation stage (Figure 7a arrows). Variations in the background wind field result in differences in the direction of the phase velocity over the 2 days (Gill, 1982). Eventually, from 04:30 UTC to 08:30 UTC on 3 March, AGWs decayed and dissipated quickly within 4 hr. The leading wave traveled forward

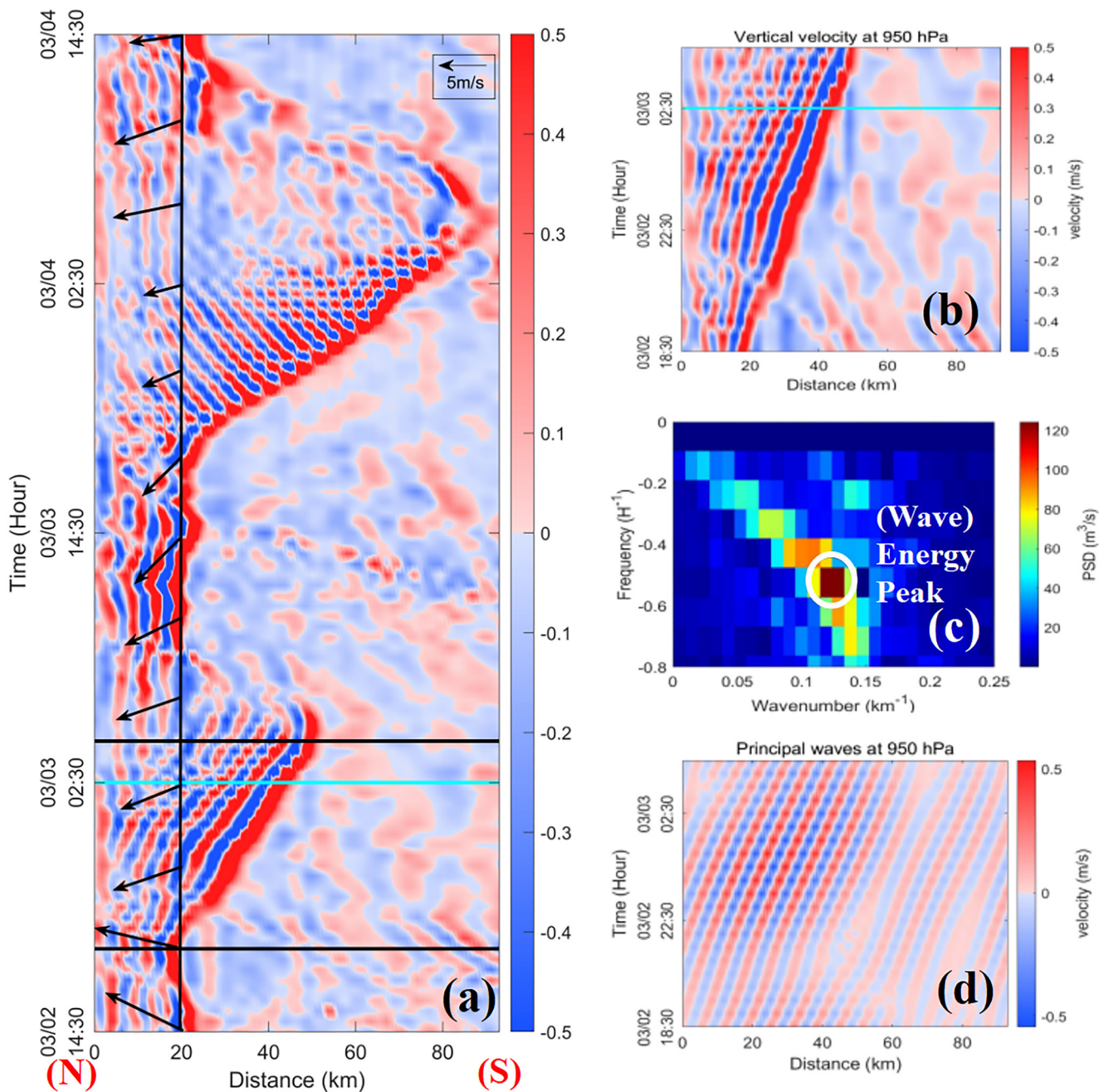


**Figure 7.** The time series of detrended wind vertical (a) at 950 hPa along the Line CD (Figure 5b) from 14:30 UTC on 2 March to 14:30 UTC on 4 March 2010. The cyan line in (a) represents the time at 02:30 UTC on 3 March, corresponding to the time of synthetic aperture radar observation (Figure 2a). The two horizontal lines in (a) frame the propagation process. The vertical black line in (a) indicates the shoreline, which serves as the starting position of propagation. The black arrows pointing left mean the 10-m height average southerly wind within 4 hr before that moment. (b) The sub-time series of propagation. (c) The 2D-spatiotemporal spectrum of (b). The white oval in (c) is situated at the peak of the spectrum. In (d), the vertical velocity is based on the principal waves within the white oval in (c).

30 km. Waves observed by SAR at 02:33 UTC were in the latter part of the offshore propagation stage. The whole process, consisting of three stages, was repeated daily from 2 March to 6 March.

To further investigate the wave propagation characteristics in one cycle of AGWs, we calculated the spatiotemporal spectrum of the propagation stage and found that the AGWs had an hour-scale wave period as propagating offshore. An example on 2 March shows that the wave period and wavelength of AGWs were 1.81 hr and 8.24 km, respectively, similar to the satellite observations. The spectral analysis indicates that the ground-relative

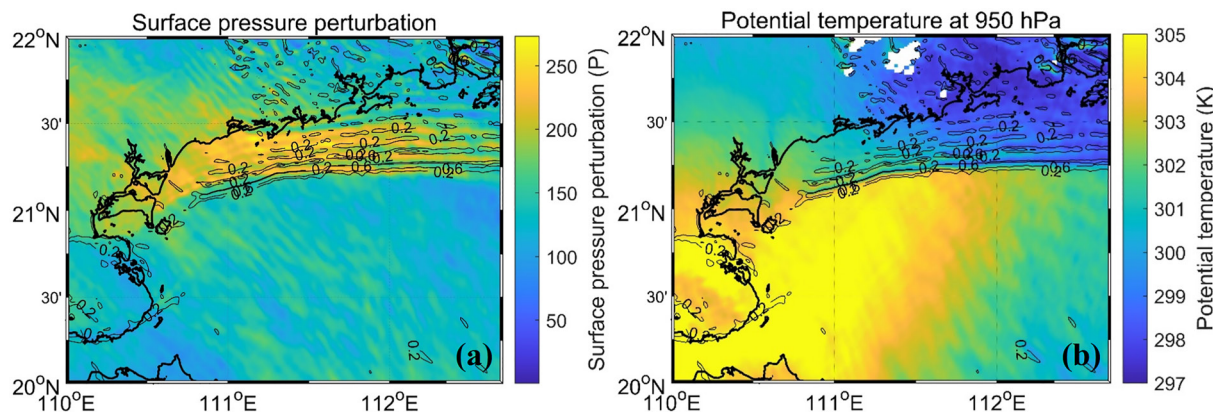


**Figure 8.** (a) Surface pressure perturbation (hPa; shading) and (b) potential temperature at 950 hPa (K; shading) at 02:30 UTC on 3 March. The contour lines represent the vertical motion at 950 hPa.

phase speed of AGWs depicted in the primary waves of Figure 7d approximated to 1.26 m/s, as can be seen in Figure 7c. Moreover, the theoretical dispersion relationship is calculated to verify the model-simulated wave spectral characteristic, which is expressed (Du et al., 2019)

$$(\omega - kU)^2 = \frac{N^2 k^2}{k^2 + m^2} \quad (1)$$

when the vertical wave number is far greater than the horizontal wave number, the dispersion relationship can be expressed as

$$\lambda_x = T \left( \frac{N \lambda_z}{2\pi} + U_b \right) \quad (2)$$

$$N = \sqrt{\frac{g \cdot d\theta}{\theta \cdot dz}} \quad (3)$$

where  $\lambda_x$  and  $\lambda_z$  represent horizontal and vertical wavelengths, respectively.  $U_b$  denotes the background wind speed.  $\theta$  is the potential temperature.  $N$  represents the Brunt–Väisälä frequency, which is used to evaluate the stability of the atmosphere (Li et al., 2013). On 3 March, the horizontal wavelength,  $\lambda_x$ , was equal to 7.14 km from the power spectrum. Meanwhile, Figure 8 shows the horizontal surface pressure perturbation and potential temperature with the vertical motions at 950 hPa at 02:30 UTC on 3 March to illustrate the polarization relationship between these three variables in AGWs during the propagation stage. The surface pressure perturbation was determined by the deviation between the surface pressure data at 02:30 UTC on 3 March and 18:30 UTC on 2 March. Figure 8a indicates that the maximum upward motion was downstream of the largest surface pressure perturbation. In Figure 8b, the maximum upward motion was located on the upstream side of the largest potential temperature. These results induced that the polarization relationship of the analyzed variables in the waves can match the basic trapped gravity wave features (Eom, 1975). Thus, the vertical wavelength can be expressed as  $\lambda_z = 4D$ , where  $D \sim 1.60$  km is the thickness of the stable layer near the surface on 3 March. Consequently,  $\lambda_z$  was equal to 6.40 km. Furthermore, the local average background wind speed,  $U_b$ , was 1.25 m/s, and the local  $N^2$  was equal to  $2 \times 10^{-4} \text{ s}^{-2}$ . As a result, the theoretical wave period was 1.58 hr, which was similar to the spectrum-based wave period of 1.81 hr. Therefore, the power spectrum can match the theoretical dispersion relationship of the AGWs.

The same spatiotemporal-spectrum method was used to find the AGWs' ground-relative phase speed was 2.43 m/s on 3 March, larger than on 2 March. The wavelengths during the propagation stages on 3 and 4 March were 8.24 and 4.71 km, respectively. Simultaneously, the corresponding southerly wind with magnitudes of  $\sim 4$  and  $\sim 8$  m/s dominated the coastal region on 3 and 4 March, respectively. The topographic characteristics of the mountains exert a pronounced blocking and lifting influence on the airflow. As a result of these localized fluctuations caused by the blocking and lifting, higher wind speeds tend to confine the fluctuations to a smaller area in the vicinity of

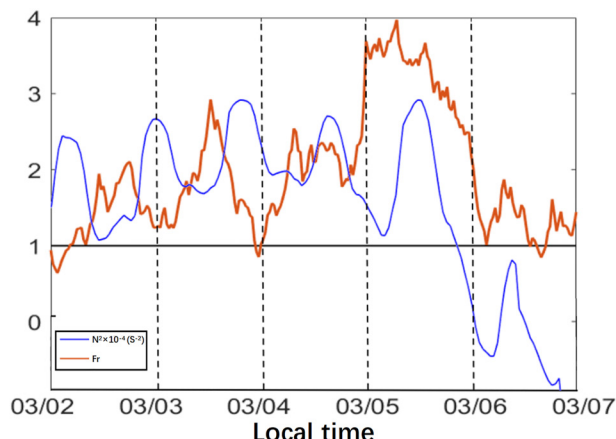


**Figure 9.** The time series of Fr and  $N^2$  along Line CD (shown in Figure 5b) is depicted for the period from 2 to 7 March at the local time. The black line represents  $Fr = 1$ .

the wave is classified as a Lee wave (Li et al., 2004). The Fr and  $N^2$  along Line CD between 2 and 7 March were shown in red and blue lines in Figure 9, respectively. Fr was equal or close to one in the local early morning of the day, indicating the upstream AGWs were generated at the beginning of the day. Moreover, during the period from the 2nd to the 6th,  $N^2$  consistently remains greater than 0, indicating an overall favoring condition for the propagation of AGWs. This conclusion is consistent with the observations.

We selected the vertical velocity profile between 2 and 3 March as an example to present upstream AGWs' development and propagation. In Figure 10a, AGWs' vertical motion reaches  $\sim 2.0$  km, implying that the upstream AGWs were generated at the lower troposphere. The amplitude of the most offshore part at 950 hPa experienced a notable increase from approximately 0.3–1.0 km during the time frame between 12:00 UTC and 18:00 UTC on 2 March, as illustrated in Figures 10a and 10b. Meanwhile, AGWs did not spread outward during this period, indicating that the AGWs were in the generation and development stage at the beginning of the day. Whereafter, AGWs propagated 20 km offshore in 6 hr against the wind direction from 18:00 UTC on 2 March to 00:00 UTC on 3 March (Figures 10b and 10c), which further indicated that this was a group of upstream AGWs. To 06:00 UTC on 3 March, AGWs further propagated offshore until complete dissipation.

To further explore the mechanisms of the upstream AGWs, we conducted a series of topography sensitivity experiments. For satisfying the upstream generation condition of AGWs, the Froude number should be close to unity. Meanwhile, the wind speed during the generation stage on 3 March is  $\sim 5\text{--}15$  m/s, and the  $N$  is about  $10^{-2}\text{--}1.6 \times 10^{-2}$  s $^{-1}$ . Consequently, the minimum terrain height required to generate the upstream wave is  $\sim 150$  m. Therefore, three topography sensitivity experiments were carried out in addition to the control group (CTRL) using the original topography. These experiments utilized the same model setup but with varying maximum mountain heights truncated at 400, 200, and 100 m, respectively. In Figure 11, the red boxes indicate the altered topographic areas surrounding Yunkai Mountain.

As the height of the artificial terrain decreases, the experimental results demonstrate a decrease in the strength and range of fluctuations in AGWs (Figure 12). In Figure 12a, the strongest fluctuation of AGWs in the simulation with original topography occurred at 02:30 UTC on 3 March, spreading to the offshore region. However, as the terrain height decreases, a weaker AGW is presented in the coastal region in Figures 12b/12c, with a maximum height of 400/200 m. It is worth noting that in Figure 12d, where the maximum height is 100 m, there is no discernible fluctuation pattern along the coastline. These sensitivity experiments corroborate the evaluation result of mountain height, indicating that the generation condition's minimum height is approximately 150 m. Thus, the sensitivity experiments demonstrate that higher topography in the Yunkai Mountain area is more favorable for AGWs' generation, indicating that the interaction between the Yunkai Mountain chain and the southerly wind is the primary mechanism of these upstream AGWs.

A similar phenomenon (Zheng et al., 2004), but not a recurring phenomenon, was observed in the same area and the same month but 10 years ago (Figure 13a). For comparison, we reprocessed the Terra image acquired at 03:40

the mountains. Overall, the AGWs in SCS show a regular periodic character, and their wave speed and wavelength relate to the magnitude of the prevailing wind speed.

## 4. Dynamic Analyses and Discussion of AGWs

### 4.1. What Are the Mechanisms of the Upstream AGWs?

To explore the AGW's upstream behavior. Froude number (Fr) is calculated as the following equation (Baines, 1998):

$$Fr = \frac{U_m}{N \cdot H} \quad (4)$$

where  $U_m$  is the mean wind speed (m/s) along the Line CD (depicted in Figure 5b), ranging from 10 m to 950 hPa, which aligns with the height of the fluctuating body.  $H$  is the mountain height, here, equal to 800 m. The generation and propagation of upstream AGWs are closely related to atmospheric stability and wind speed. When Fr is close to 1.0, and the wind direction is opposite to the direction of wave propagation, the atmospheric condition is favorable for the upstream gravity wave (Baines, 1977, 1998). Otherwise,

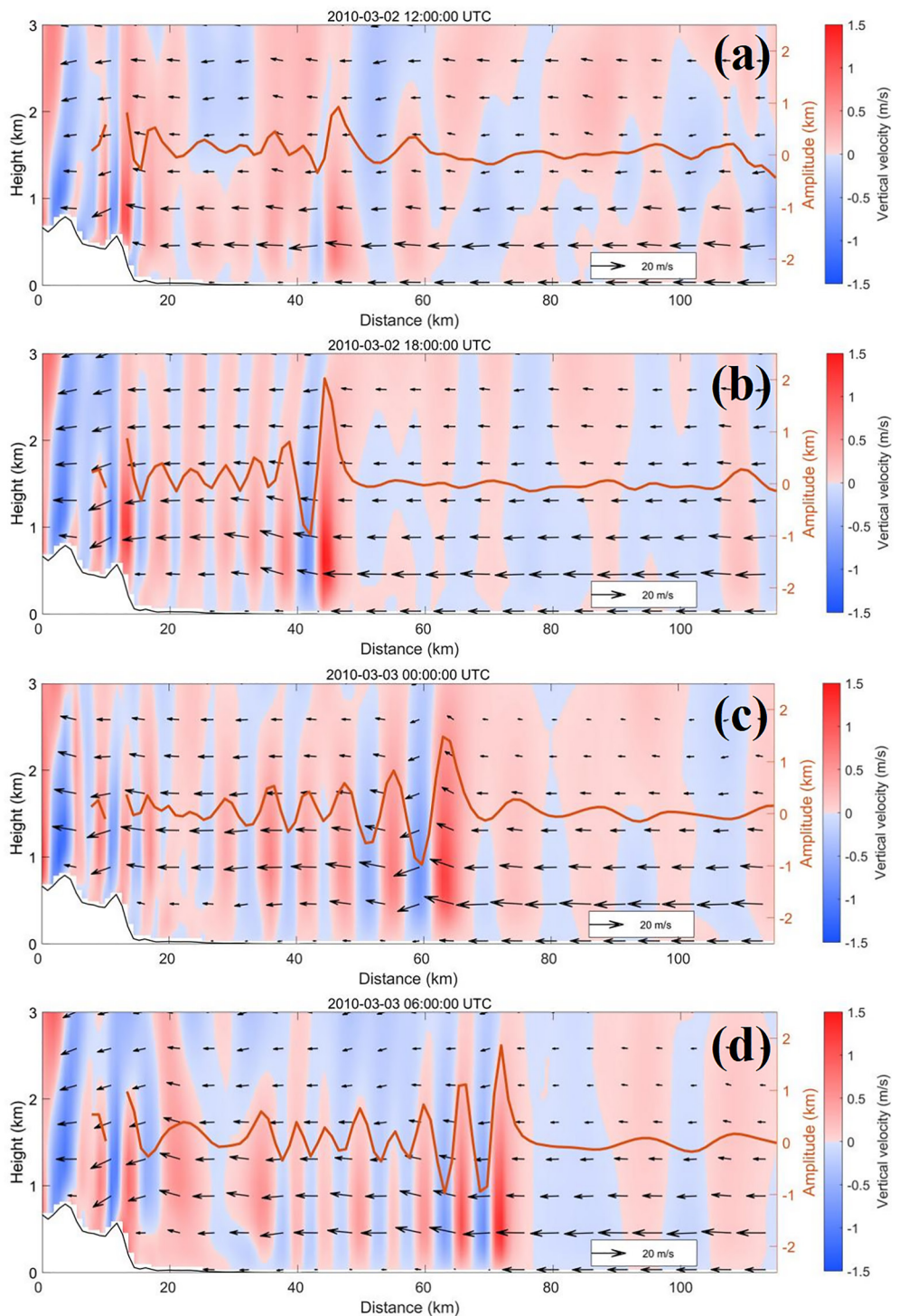


**Figure 10.** The wind vertical velocity profiles with the wind vectors and wave amplitudes at 950 hPa along the Line CD (shown in Figure 5b) at 12:00:00 UTC (a) and 18:00:00 UTC (b) on 2 March, at 00:00:00 UTC (c) and 06:00:00 UTC (d) on 3 March. The vertical component of the wind vectors was multiplied by 10. The thin black curves denote the topography. The red lines indicate the fluctuation of the waves.

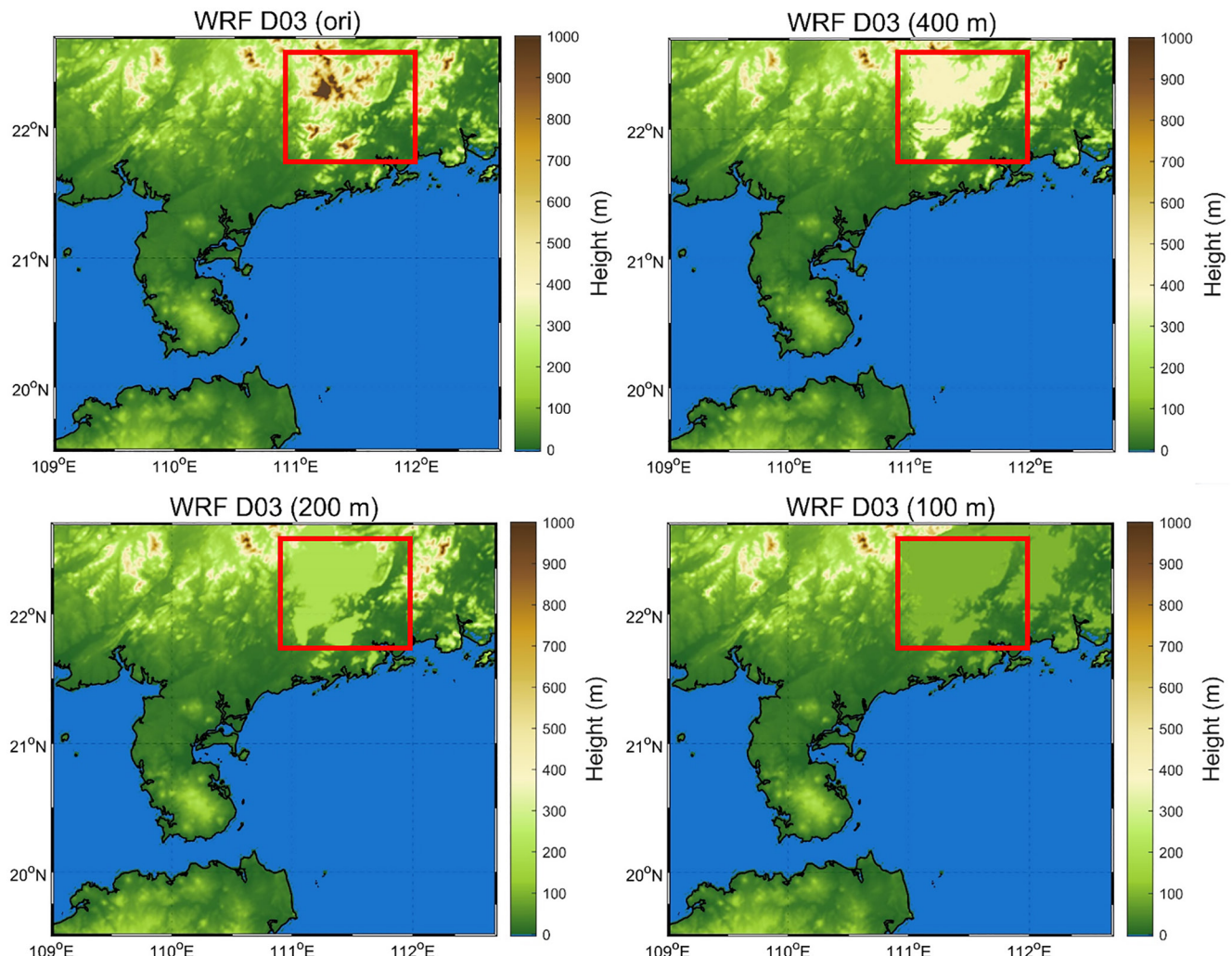


**Figure 11.** Topographic height for sensitivity experiments.

UTC on 5 March 2010, to present a similar AGW pattern to the southwest side of Hainan Island. The similar wavelike form and different wave direction between the cases in this study and Zhang's study suggest that Hainan Island can also act as a disturbance source to modulate this upstream AGW. Hence, the additional potential disturbance sources are analyzed to evaluate the coastal upstream AGWs systematically.

An experimental simulation using a larger WRF domain 03 is designed and implemented, which covered the entire Hainan Island. We examined the spatiotemporal changes in vertical velocity along the Line GH on 4 March 2010, similar to the cross line used in Zheng et al. (2004) (shown in Figure 13a). Figure 14 presents the vertical velocity profiles along the Line GH at 18:00 UTC on 4 March (generation stage) and 00:00 UTC on 5 March (propagation stage). At 18:00 UTC on 4 March (Figure 14a), two distinct fluctuations, Wave 1 and Wave 3, were generated on the landside and seaside of the Yunkai Mountain joint area, respectively. Meanwhile, another independent fluctuation, Wave 2, was also generated at Hainan Island. The distance between Waves 1 and 2 is more than 250 km. After 6 hr of propagation, at 00:00 UTC on 5 March (Figure 14b), the distance between Wave 1 and Wave 2 was near ~200 km. As a result, Wave 2-related downstream wave train from Hainan Island had some influence on the upstream Wave 1 on the right side of the Leizhou Peninsula (Figure 14b black box).

From the MODIS image, some fluctuations different from the upstream waves (Wave 1) can be observed at the land-sea interface (Wave 3 in Figure 13b red box). And the findings in the 100 m terrain sensitivity experiment also demonstrate that a gravity wave phenomenon (bores) persists exclusively in the landward region (Figure 12d red box) when there is no Yunkai Mountain. The results of the terrain sensitivity experiments reveal

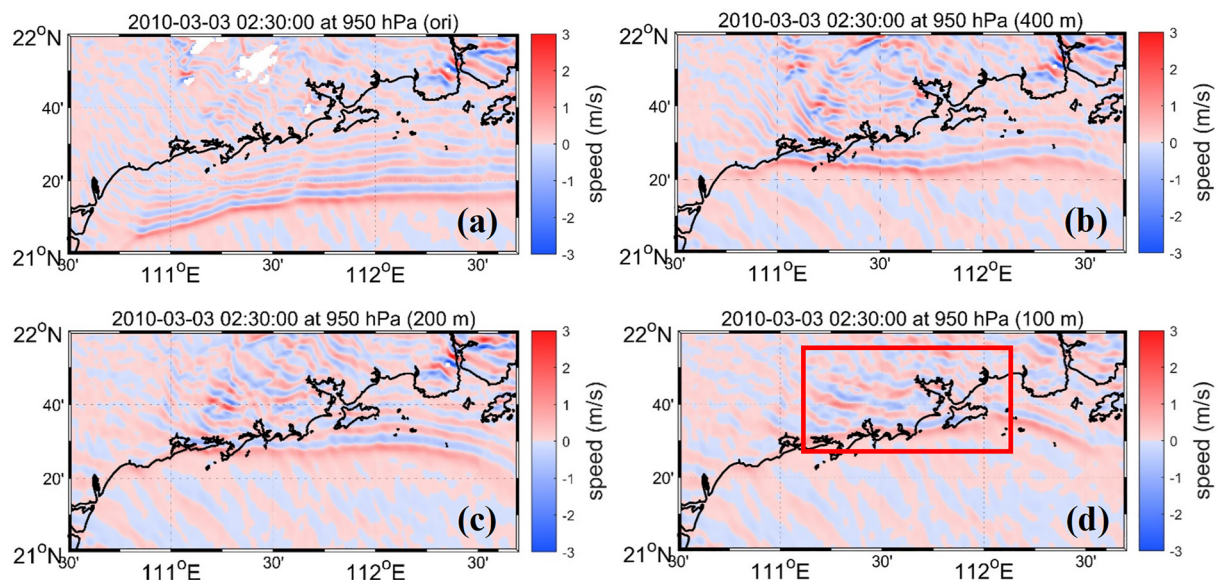


**Figure 12.** The Weather Research and Forecasting simulated vertical wind velocity for sensitivity experiments.

that background wind fields show similar trends over the land in the generation stage, even without considering Yunkai Mountain (Figures 15a and 15b red boxes). In the sensitivity experiment without Yunkai Mountain, the southerly winds demonstrate higher speeds over the ocean, whereas they decrease sharply over land. This phenomenon results in a conspicuous wind speed gradient at the land-sea interface, resembling the characteristics of a land (mountain) breeze. Thus, the occurrence of bores phenomena should attribute to the abrupt wind speed variations in the land-sea interface (Haghi & Durran, 2021; Mueller et al., 2017). However, these bores cannot develop into the satellite-observed upstream AGW phenomenon over the sea surface, further indicating that bores were not the main factor in this study area.

In summary, the results of sensitivity experiments indicate that these upstream AGWs (Wave 1) along the coast were triggered due to the southerly wind and mountain interaction. Namely, the AGWs observed on the east side of the Leizhou Peninsula were topography-induced tropospheric upstream gravity waves. Li reported a similar finding in 2004 (Li et al., 2004). Furthermore, the fluctuation (Wave 2) from Hainan Island and the undular bores (Wave 3) caused by the abrupt wind speed variations in the land-sea interface modulate these upstream AGWs (Wave 1).

#### 4.2. The Vertical Structure of Upstream Waves and Associated Environmental Factors

To explore the propagation environment of the upstream AGWs, we calculated the Scorer  $I^2(z)$  ( $\text{m}^{-1}$ ) to identify favorable wave propagation conditions. Scorer number is described as (Li et al., 2011; Valkonen et al., 2010)

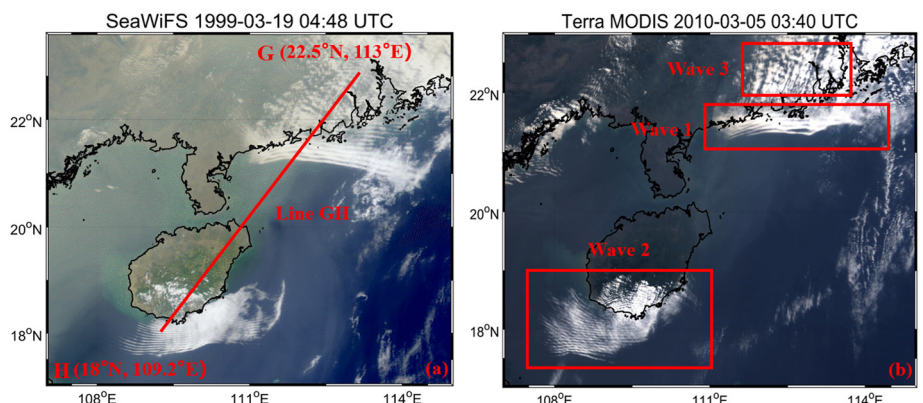


**Figure 13.** (a) A true color SeaWiFS image taken on 19 March 1999. (b) A true color Terra image taken on 5 March 2010.

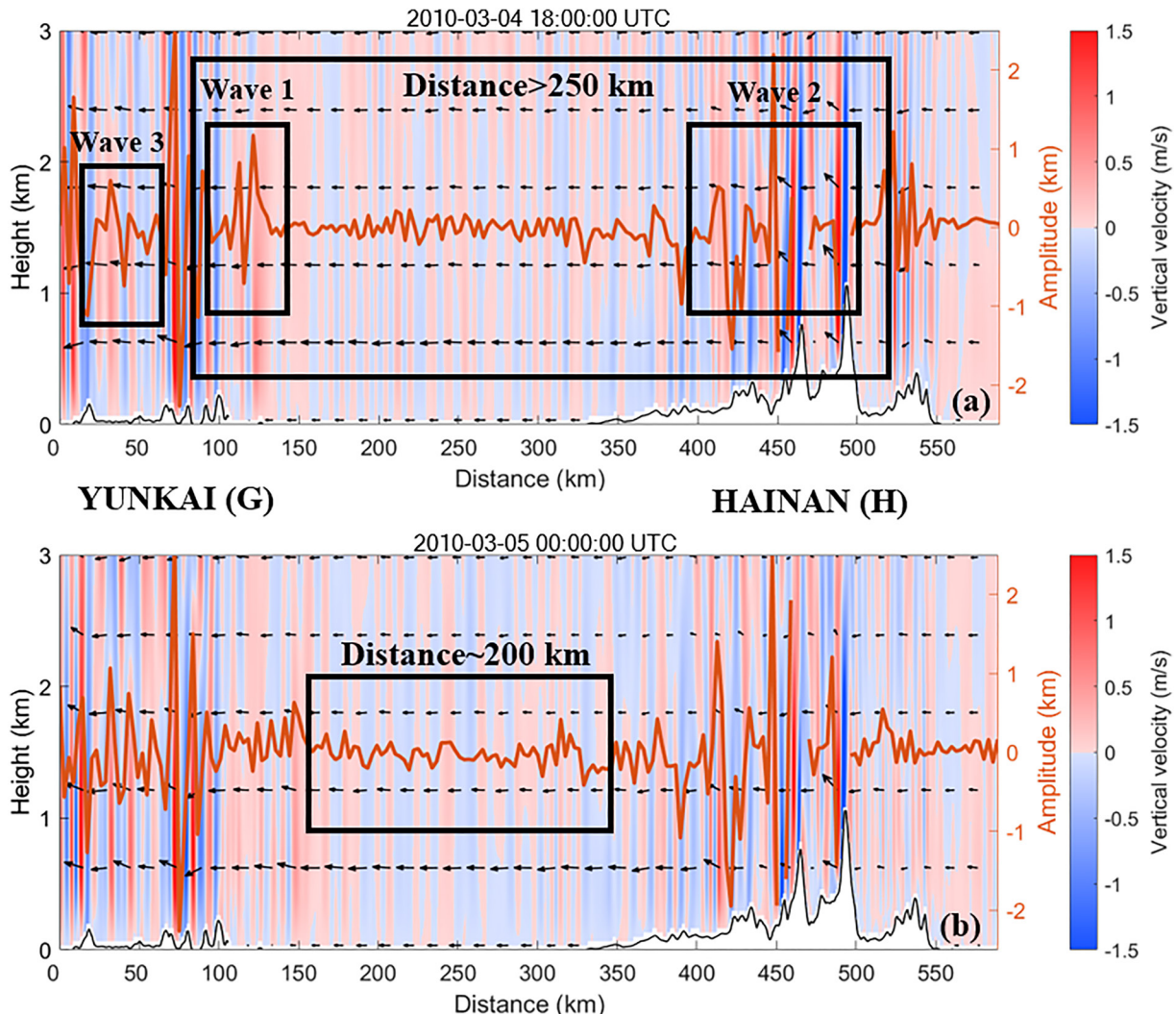


**Figure 14.** The wind vertical profiles with the wind vectors and wave amplitudes at 950 hPa along the Line GH (shown in Figure 13a) at 18:00:00 UTC (a) on 4 March and at 00:00:00 UTC (b) on 5 March.

$$l^2(z) = \frac{N^2}{(U - C)^2} - \left( \frac{\partial^2 U}{\partial Z^2} / (U - C) \right) \quad (5)$$

where  $U=U(z)$  is the vertical profile of the horizontal wind. Decreasing  $l^2(z)$  with height means the atmospheric condition is favorable for trapped AGWs to propagate horizontally. Oppositely, a near constant  $l^2(z)$  with height or increasing  $l^2(z)$  with height indicates that AGWs will propagate vertically. The vertical profiles of Scorer number along the Line CD based on WRF results at 12:00 UTC and 18:00 UTC on 2 March and 00:00 UTC and 06:00 UTC on 3 March are shown in Figure 16 shading. The thin bottom lines in Figure 16 represent the topographic features along the Line CD, with a hill (attached to the Yunkai Mountains) over 800 m above sea level about 30 km from the coastline. The southerly wind blowing this hill caused a change in wind speed and Brunt-Väisälä frequency associated with the Scorer number (Qing et al., 2008). Meanwhile, Scorer number decreased from near the surface to over 800 m in height at 18:00 UTC on 2 March and 00:00 UTC on 3 March (Figures 16b and 16c shading), showing that waves can horizontally propagate. In Figure 16d, the vertical black lines indicate the average Scorer number along the Line CD in the region of 60–80 km from the coastal edge at 06:00 UTC on 3 March, which corresponds to the location of upstream AGWs dissipation in the local afternoon. In the dissipate phase, as height increases below 2 km, there is an increasing tendency for the Scorer number, indicating that the environment is no longer favorable for propagation during this period (Figure 16d yellow boxes). The brown

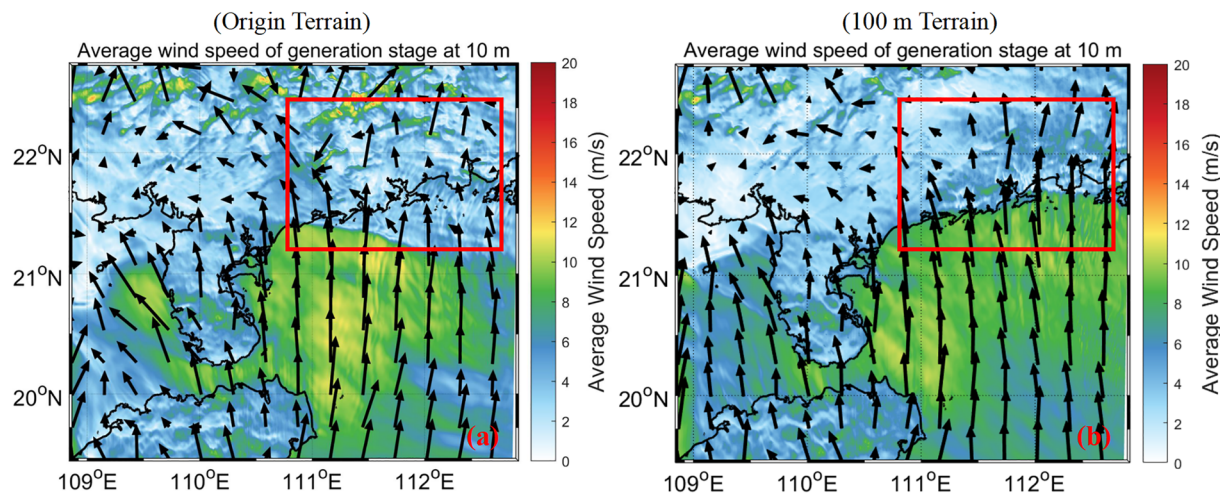


**Figure 15.** The average wind speed at 10 m during the generation stage (12:30 UTC to 18:30 UTC on 2 March) with the origin terrain (a) and no Yunkai Mountain terrain (b).

lines in Figure 16 indicate the air temperature at 33 m height, the bottom level in the model output, along Line CD. Figure 16a represents the generation stage of the process, with the temperature elevated by 2°C from 23°C (nearly the coast) to 25°C (70 km offshore). Figures 16b and 16c represent the propagation stage; the sea-coast temperatures are close in this stage with a minimum value of 22.5°C. In Figure 16d, the decay and dissipation of AGWs were caused by the strongest solar radiation in the local afternoon when the air temperature rose to induce the thickening of the mixed layer near the sea surface. The average thickness of the PBL for AGWs in the offshore region is approximately 240 m during the propagation stage and 280 m during the dissipation stage. Furthermore, the average Brunt-Väisälä frequency below 2 km height decreased from  $N^2 = 4.3 \times 10^{-4} \text{ s}^{-2}$  at 00:00:00 UTC to  $N^2 = 3.2 \times 10^{-4} \text{ s}^{-2}$  at 06:00:00 UTC, leading to a weak instability below 2 km height. As a result, the AGWs gradually dissipated in the local afternoon. After the dissipating stage, the air temperature decreased with the AGWs' reinforcement on the east side of the Leizhou Peninsula again in the local nighttime.

In addition to Scorer number, the existence of a wave ducting layer is another critical condition to modulate the propagation of the waves. There are three criteria to examine a wave ducting layer (Du & Zhang, 2019; Lindzen & Tung, 1976).

1. Three layers exist in the troposphere, with different static stabilities (a near-surface stable layer, a middle-level less stable layer, and a top stable layer).
2. The ground-relative phase speed of waves equals the background wind speed in the wave propagation direction.
3. The small Richardson number ( $Ri$ ) in the middle level is a less stable layer ( $Ri < 0.25$ ).

According to these three criteria of the wave ducting layer, we analyze the stability along the vertical profile of the atmosphere. The Richardson number is used to evaluate atmospheric stability (Li et al., 2013).

$$Ri = \frac{N^2}{\left(\frac{\partial U}{\partial z}\right)^2} \quad (6)$$

The vertical profile of Brunt-Väisälä frequency in the propagation stage along Line EF (Figure 3a) is shown in Figure 17a. As shown, in the propagation stage,  $N^2$  is large below the  $\sim 1.2 \text{ km}$  ( $N^2 > 1 \times 10^{-4} \text{ s}^{-2}$ ), and this layer is relatively stable;  $N^2$  at a relatively small value (nearly 0) at  $\sim 1.2\text{--}2.8 \text{ km}$  and this layer is not stable; Above 2.8 km, the  $N^2$  increases and the layer stable again. Thus, three layers exist with different static stabilities in the troposphere (Criterion 1 was satisfied). The calculated wave phase speed was  $\sim 1.26 \text{ m/s}$  in the propagation stage. Simultaneously, the wind speed at the steering level ( $\sim 2.5 \text{ km}$ ) was  $\sim 1.3 \text{ m/s}$  in the wave propagation direction (red circle in Figure 17b), which was close to the wave phase speed. Thus, criterion 2 was satisfied. In Figure 17c, the range of  $Ri < 0.25$  mainly exists between 1.5 and 2.5 km, matching the AGW's amplitude. Thus, criterion 3 was satisfied. As a result, there was a wave ducting layer conducive to AGWs' propagation below 2.5 km during the study period.

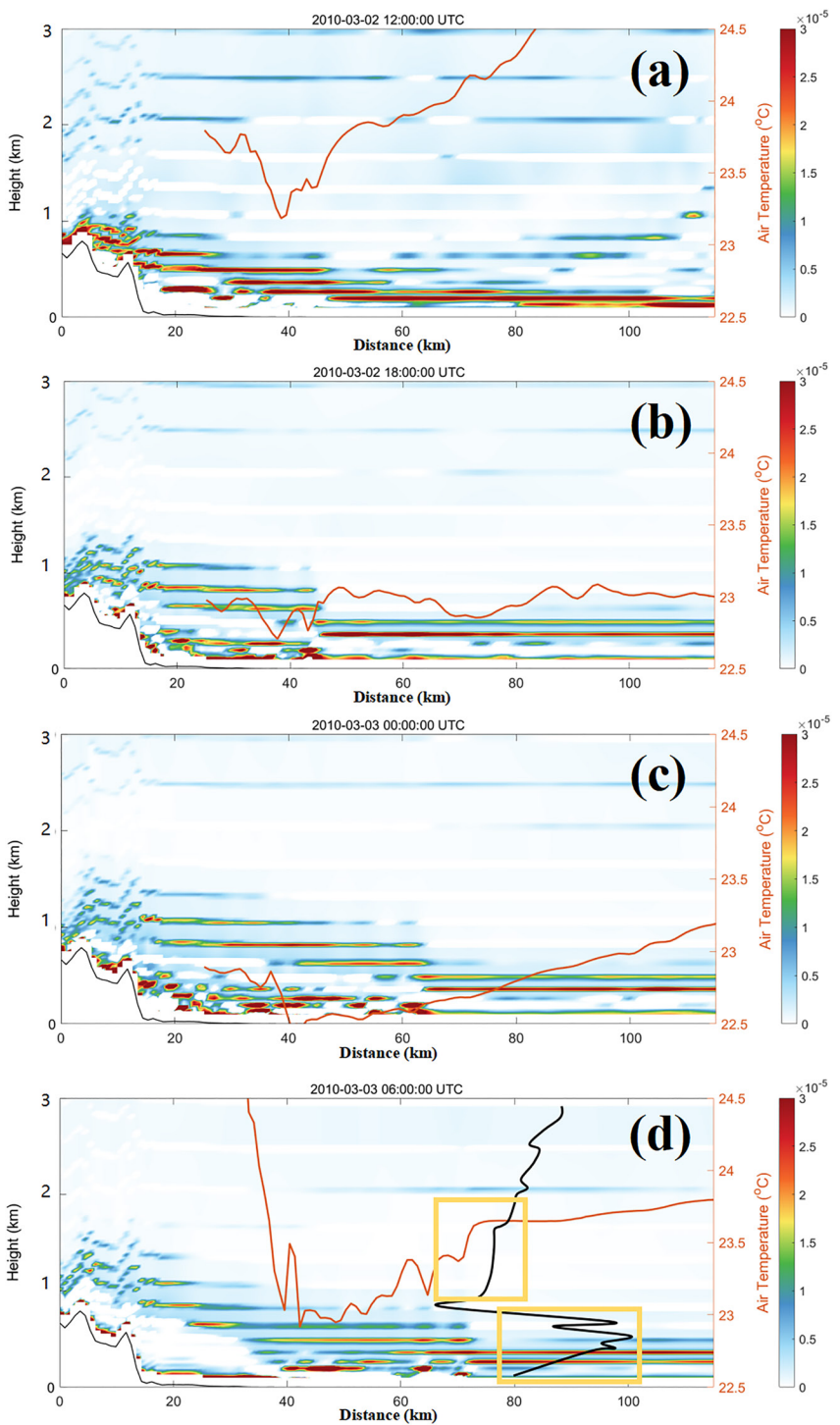


**Figure 16.** The 33 m height air temperature (red lines) and the Scorer profiles below 3 km height (shading) along the Line CD (Figure 5b) at 12:00:00 UTC (a) and 18:00:00 UTC (b) on 2 March, at 00:00:00 UTC (c) and 06:00:00 UTC (d) on 3 March, respectively. The thin black lines at the bottom of the Figures (a–d) were the land topography along the Line CD. The vertical black line in (d) represents the mean vertical profiles of Scorer values within a range of 60–80 km from the coastline during the dissipating stage.

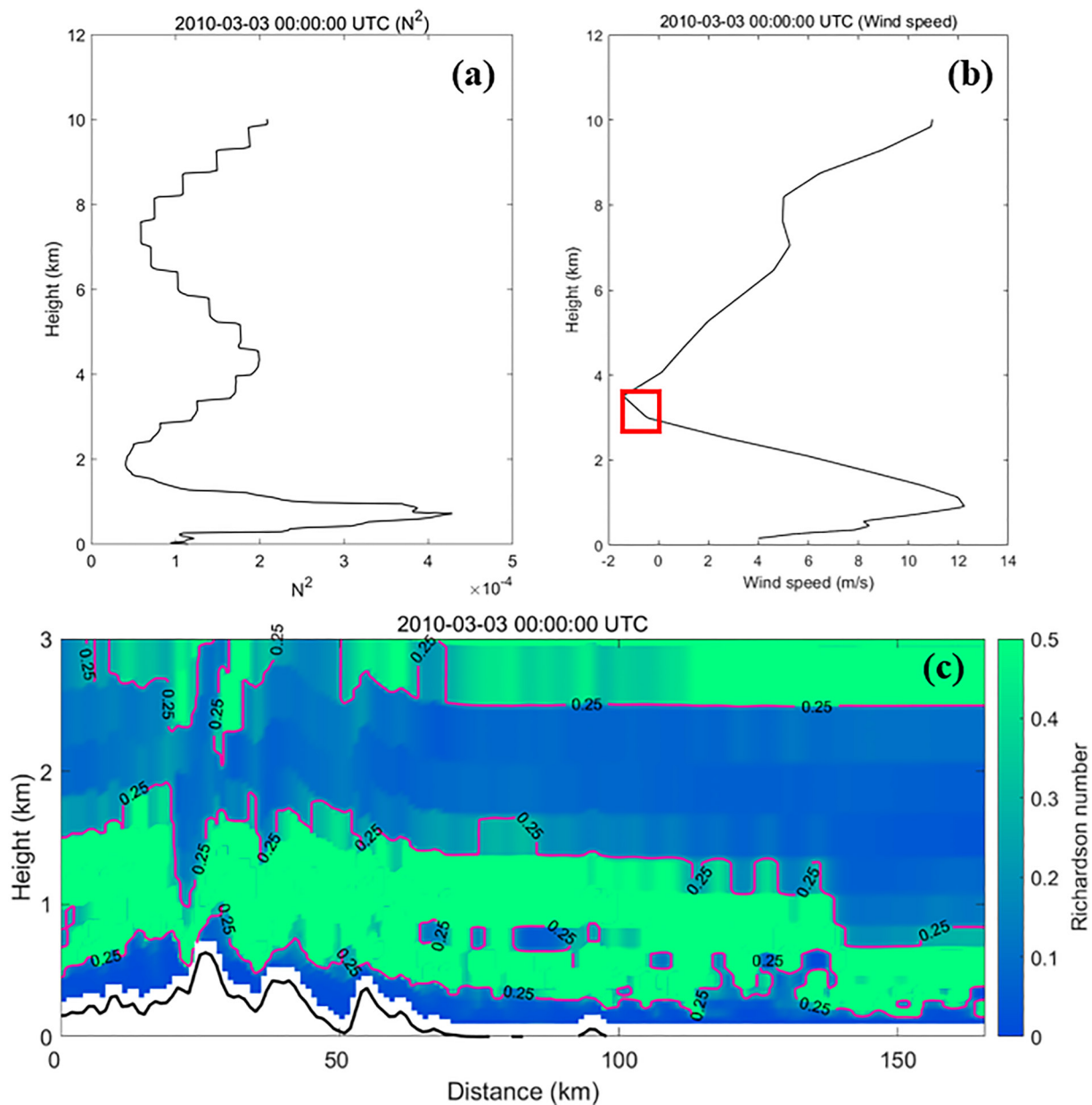


**Figure 17.** (a) Illustrates the average vertical profile of the square of Brunt–Väisälä frequency along the Line EF (shown in Figure 3a) at 00:00:00 UTC on 3 March. (b) Shows the mean wind speed profile along the Line EF in the direction of wave propagation. (c) Displays the profile of the Ri along the Line EF (contour). The red lines in (c) marks the  $Ri = 0.25$ .

Combined analysis of the Scorer number, Froude number, Richardson number, and wave ducting layer confirmed that the upstream AGWs existed in the SCS from 2 to 6 March, which is consistent with the satellite observations (shown in Figure 3). In addition, there was a wave ducting layer below 2.5 km during the study period, which is in favor of the AGWs propagation.

#### 4.3. What Caused the Rarity of This Recurring Phenomenon?

To further analyze the reasons for this rare phenomenon, we expressed a variant Brunt–Väisälä frequency ( $N_v$ ) as an equation of temperature bias and temperature (Neale et al., 2010)

$$N_v^2 = \left( \frac{g^2}{c_p} \right) \cdot \left( \frac{1}{T} \right) \cdot \left[ 1 - K \cdot \left( \frac{1}{T} \right) \cdot \Delta T \right] \quad (7)$$

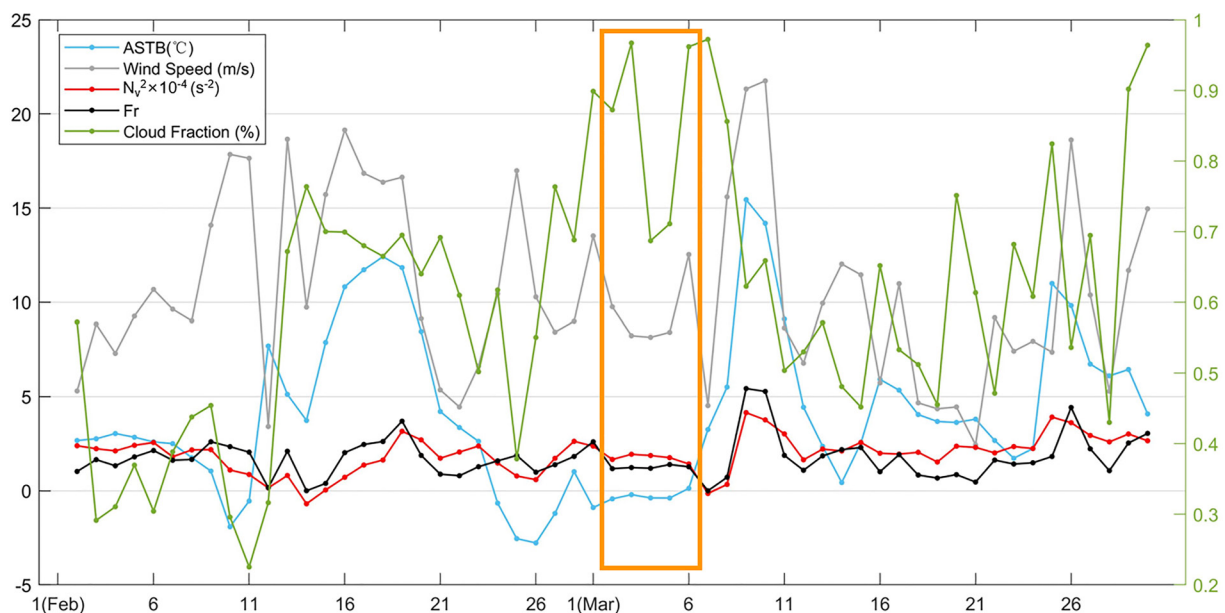


**Figure 18.** The atmosphere-sea temperature bias of air surface to 800 m above the sea from 1 February to 31 March 2010, is shown in the blue line. The sea surface wind speed is represented by the gray line, while the averages of  $N_v^2$  and Fr along Line CD are indicated by the red and black lines, respectively. These four variables share the left axis. Additionally, the total cloud cover fraction is depicted by the green line, corresponding to the right axis. The orange box marks 2 to 6 March.

where  $K$  has a desirable constant of 44.70 on a specified isobaric surface 925–1,000 hPa.  $C_p$  is the constant pressure specific heat,  $C_p = 1,004.5 \text{ J/kg K}$ .  $T$  is the air temperature and  $\Delta T$  is the variation of air temperature in the vertical direction. Based on the rapidly changing characteristics of the atmosphere, the ERA5 reanalysis hourly data from 1 February to 31 March, covering the recurring AGWs event, is used to analyze the relevant background field variables including pressure, wind speed, cloud fraction, and atmosphere-sea temperature bias (ASTB). The changing trends are shown in Figure 18. The blue line represents the temperature bias between the sea surface and 800 m (ASTB), and for all the ASTBs recorded from 2 March to 6 March, the values are approximately 0. This indicates that the temperature difference in the vertical direction is relatively small during this particular period. The gray line is wind speed indicating that considerable wind speed is important for the occurrence of these AGWs. The red line shows the  $N_v^2$  is relatively stable around  $2 \times 10^{-4} \text{ s}^{-2}$ , which means the lower atmosphere is stable for AGWs' generation and propagation. The Fr during the generation stage is shown in the black line. The Fr was around 1 from 2 to 6 March, indicating that the atmospheric environment was favorable for generating upstream AGWs.

Overall, between 2 and 6 March, 2010, the special temperature difference (nearly 0) was an important background field factor distinguishing from other dates that caused the atmospheric formation to stabilize. Thus, the upstream AGWs can be generated and propagated easily. Meanwhile, the green line in Figure 18 indicates that the cloud content from 2 to 6 March is greater than 50%. Adequate cloud content is also important for satellites to capture these wave-like features (Astafurov & Skorokhodov, 2017).

The ERA-5 hourly mean temperature at 950 hPa in the AGWs generation stage was used to explore the reasons for the rarity of the AGWs days. To emphasize the specificity of these upstream AGWs, we plot the average temperature fields at 950 hPa height for the generation stage of 2 to 7 March (Figures 19a–19f). Also, we plotted the average temperature field for the whole month of March in 2010 (Figure 19g). By comparing these temperature fields, we can gain a deeper comprehension of the exceptional nature of the AGWs' occurrence during the period of 2 to 6 March. From 2 to 6 March (Figures 19a–19e), the result indicated a collision occurred between warm air from the southwest and cold air from the northeast in southern China. The study area, located to the east of the Leizhou Peninsula, was situated in the warm air region, with temperatures at 950 hPa ranging from 295 to 300 K. The presence of warm air contributed to the stability of the air temperature above the ocean. On 7 March (Figure 19f), when cold air infiltrated the study area, the temperature dropped by 10 K to 285–290 K. Consequently, the AGWs disappeared on 7 March. The decrease in air temperature led to a decrease in buoyancy

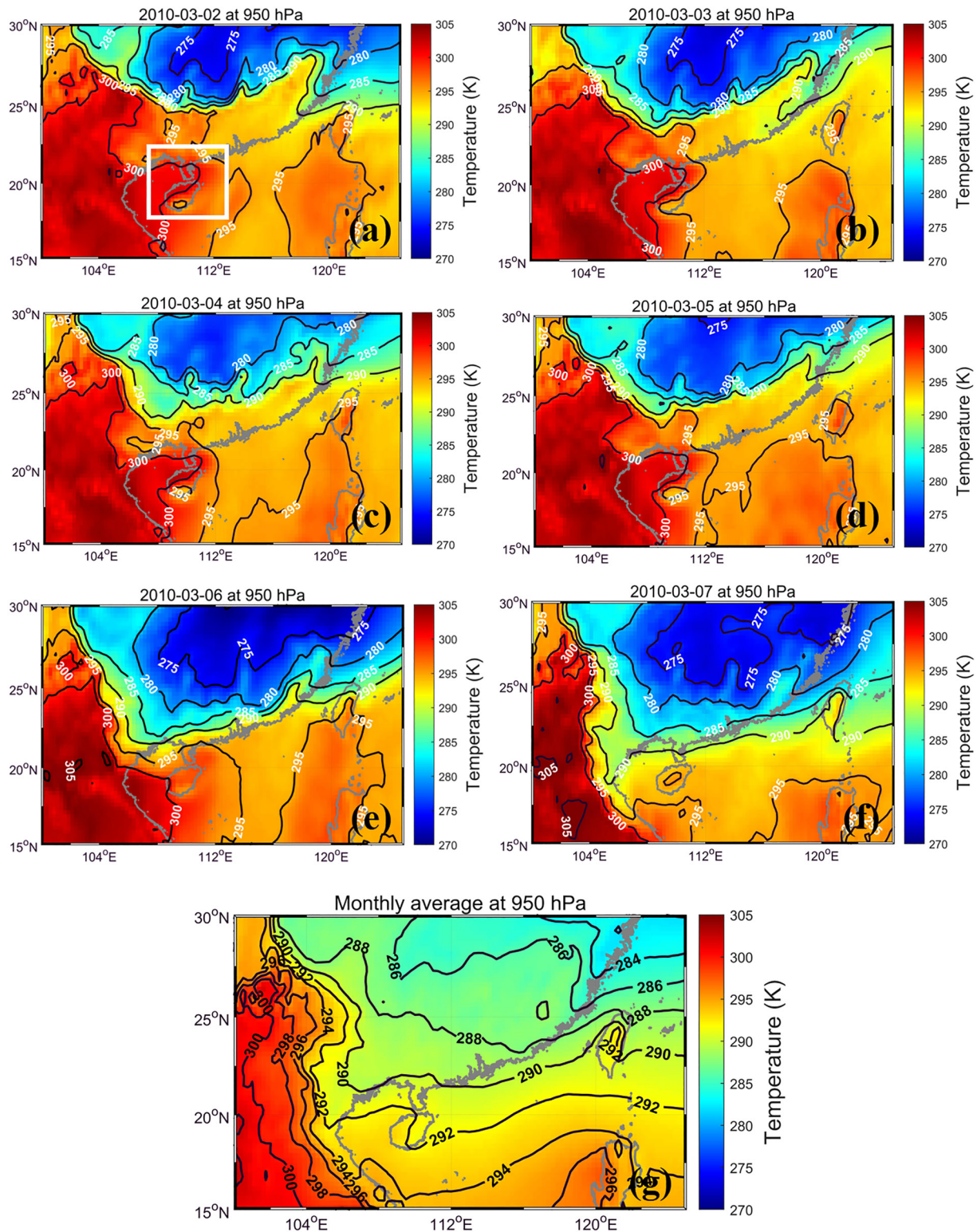


**Figure 19.** Figures (a)–(f) show the mean temperature during AGWs' generation and propagation stages from 2 to 7 March. The black lines represent the isobars, and the white box in (a) marks the study area. Additionally, (g) displays the monthly average mean temperature for March, with the black line representing the monthly average isobar.

frequency ( $N_v^2$ ) (orange box in Figure 18), rendering the environment unsuitable for upstream AGWs. Thus, the presence of the warm air masses from the west between 2 and 6 March provided a suitable environment for the generation and propagation of the upstream AGWs.

## 5. Conclusions

Recurring AGWs were captured by both SAR and MODIS on the east side of the Leizhou Peninsula in the northern SCS from 3 to 6 March 2010. To understand the uniqueness of the recurring AGWs phenomenon, the triple nested domains of the 9-3-1 km spatial resolutions were exploited based on one of the numerical atmospheric model, known as WRF. It was implemented to simulate these AGWs on the east side of the Leizhou Peninsula between 2 and 7 March 2010. As a result of the above models 2D-FFT method, Scorer number, Froude number and Richardson number were employed to analyze the spatiotemporal characteristics and dynamics mechanisms of AGWs. The experimental results of this study are summarized as the followings:

1. These recurring AGWs were upstream waves induced by the wind-mountain interaction. The interaction between the south-originated wind (5–15 m/s) and the Yunkai Mountain chain (~800 m height) was the main cause of the upstream AGWs along the coast, while wave fluctuations from Hainan Island and bores at the land-sea interface had partially contributed to modulating the upstream AGWs. The WRF-simulated Froude number (Fr) time series shows the upstream propagation phenomena was triggered when Fr equals 1 from late night to morning. With an altitude of lower than 1 km, the Scorer number decreased dramatically, indicating that the AGWs were most likely generated in the lower troposphere.
2. The wave period and wavelength of AGWs were 1.81 hr and 8.24 km derived by spatiotemporal spectrum. The average phase speed was approximately 1.26 m/s within the vital observation of SAR, and the amplitude was up to 2 km. Furthermore, these AGWs lead to a recurring period of about 18 hr with three variation stages: generation, offshore propagation, and dissipation. The magnitude of the wind speed in the generation stage was dependent on the phase speed of AGWs. For this specific region of SCS, upstreams are more likely to be generated late at night when the air temperature is low and propagated from early morning to the next day's high noon (18:30 UTC to the next day 04:30 UTC). Meanwhile, there was a wave ducting layer i.e., conducive to AGWs propagation below 2.5 km during this period. Solar radiation and air temperature increase when sunrises intensify the disturbance and mixing of the atmospheric boundary layer. As a result, the mixing and instability trend of the low-layer atmosphere gives rise to the dissipation of AGWs in the afternoon, particularly between 04:30 UTC and 08:30 UTC.
3. This particular case occurred during a period from 2 to 6 March when warm air from the southwest and cold air from the northeast confronted above the SCS. The collision of these air masses was considered the main reason for the creation of this unique event. The confrontation of cold and warm air masses kept the Leizhou Peninsula in the warm air mass area with a small air-sea temperature difference on 2 March. This phenomenon continued until 6 March; the event eventually disappeared due to a large invasion of cold air masses, resulting in a larger temperature difference between the sea and air. At the same time, sufficient cloud content (>50%) is the key criterion for MODIS to capture the existence of AGWs.

## Data Availability Statement

The Envisat ASAR image (European Space Agency, 2021) was downloaded from <https://esards.eo.esa.int/oads/access/collection/>. The MODIS images (MODIS Characterization Support Team (MCST), 2017) were from <https://ladsweb.modaps.eosdis.nasa.gov/>. The ERA-5 hourly data were downloaded from Copernicus Climate Change Service (C3S) Climate Data Store (CDS) (Copernicus Climate Change Service & Climate Data Store, 2023) <https://cds.climate.copernicus.eu/cdsapp/>. The CCMP Version-3.0 vector wind analyses (Mears et al., 2022) are produced by Remote Sensing Systems. Data are available at <https://www.remss.com/measurements/ccmp/>. The NCEP Climate Forecast System Reanalysis (CFSR) 6-hourly Products (Saha et al., 2010) data were downloaded from the Research Data Archive at the National Center for Atmospheric Research, Computational and Information Systems Laboratory at <https://rda.ucar.edu/datasets/ds093.0/>.

## Acknowledgments

This work was supported by the major project of the Strategic Priority Research Program of the Chinese Academy of Sciences (XDA19060101, XDB42000000), Major scientific and technological innovation projects in Shandong Province (2019JZZY010102), the CAS Program (Y9KY04101L).

## References

- Astafurov, V., & Skorokhodov, A. (2017). Identification of atmospheric gravity waves in clouds over a water surface from MODIS imagery. *Atmospheric and Oceanic Optics*, 30(1), 44–49. <https://doi.org/10.1134/s102485601701002x>
- Baines, P. G. (1977). Upstream influence and Long's model in stratified flows. *Journal of Fluid Mechanics*, 82(1), 147–159. <https://doi.org/10.1017/s0022112077000573>
- Baines, P. G. (1998). *Topographic effects in stratified flows*. Cambridge University Press.
- Bretherton, F. P. (1969). Momentum transport by gravity waves. *Quarterly Journal of the Royal Meteorological Society*, 95(404), 213–243. <https://doi.org/10.1002/qj.49709540402>
- Chunchuzov, I., Vachon, P., & Li, X. (2000). Analysis and modeling of atmospheric gravity waves observed in RADARSAT SAR images. *Remote Sensing of Environment*, 74(3), 343–361. [https://doi.org/10.1016/s0034-4257\(00\)00076-6](https://doi.org/10.1016/s0034-4257(00)00076-6)
- Copernicus Climate Change Service, Climate Data Store. (2023). ERA5 hourly data on single levels from 1940 to present [Dataset]. Copernicus Climate Change Service (C3S) Climate Data Store (CDS). Retrieved from <https://cds.climate.copernicus.eu/cdsapp#!/dataset/reanalysis-era5-single-levels>
- Da Silva, J., Ermakov, S., Robinson, I., Jeans, D., & Kijashko, S. (1998). Role of surface films in ERS SAR signatures of internal waves on the shelf: 1. Short-period internal waves. *Journal of Geophysical Research*, 103(C4), 8009–8031. <https://doi.org/10.1029/97jc02725>
- Du, Y., Rotunno, R., & Zhang, F. (2019). Impact of vertical wind shear on gravity wave propagation in the land-sea-breeze circulation at the equator. *Journal of the Atmospheric Sciences*, 76(10), 3247–3265. <https://doi.org/10.1175/jas-d-19-0069.1>
- Du, Y., & Zhang, F. (2019). Banded convective activity associated with mesoscale gravity waves over southern China. *Journal of Geophysical Research: Atmospheres*, 124(4), 1912–1930. <https://doi.org/10.1029/2018jd029523>
- Eckermann, S. D., & Vincent, R. A. (1993). VHF radar observations of gravity-wave production by cold fronts over southern Australia. *Journal of the Atmospheric Sciences*, 50(6), 785–806. [https://doi.org/10.1175/1520-0469\(1993\)050<0785:roqgwg>2.0.co;2](https://doi.org/10.1175/1520-0469(1993)050<0785:roqgwg>2.0.co;2)
- Ek, M., Mitchell, K., Lin, Y., Rogers, E., Grunmann, P., Koren, V., et al. (2003). Implementation of Noah land surface model advances in the National Centers for Environmental Prediction operational mesoscale Eta model. *Journal of Geophysical Research*, 108(D22), 8851. <https://doi.org/10.1029/2002jd003296>
- Eom, J. K. (1975). Analysis of the internal gravity wave occurrence of 19 April 1970 in the Midwest. *Monthly Weather Review*, 103(3), 217–226. [https://doi.org/10.1175/1520-0493\(1975\)103<0217:aotigw>2.0.co;2](https://doi.org/10.1175/1520-0493(1975)103<0217:aotigw>2.0.co;2)
- Ertekin, R. C., Qian, Z. M., & Wehausen, J. V. (1990). Upstream solitons and wave resistance. In G. T. Yates (Eds.), *Engineering science, fluid dynamics*.
- European Space Agency. (2021). Envisat ASAR wide swath medium resolution L1 product. IPF version 6.03 [Dataset]. <https://doi.org/10.5270/EN1-4c37krv>
- Evdoshenko, M. (2016). Detecting imprints of atmospheric waves in the Bering Sea with MODIS data. *Oceanologia*, 58(4), 264–271. <https://doi.org/10.1016/j.oceano.2016.04.003>
- Francis, S. H. (1975). Global propagation of atmospheric gravity waves: A review. *Journal of Atmospheric and Terrestrial Physics*, 37(6–7), 1011–1054. [https://doi.org/10.1016/0021-9169\(75\)90012-4](https://doi.org/10.1016/0021-9169(75)90012-4)
- Gan, X., Huang, W., Li, X., Chen, X., Lou, X., Zhao, Z., et al. (2008). Coastally trapped atmospheric gravity waves on SAR, AVHRR and MODIS images. *International Journal of Remote Sensing*, 29(6), 1621–1634. <https://doi.org/10.1080/01431160701395260>
- Gill, A. E. (1982). *Atmosphere-ocean dynamics*. Academic Press.
- Haghi, K. R., & Durran, D. R. (2021). On the dynamics of atmospheric bores. *Journal of the Atmospheric Sciences*, 78(1), 313–327. <https://doi.org/10.1175/jas-d-20-0181.1>
- Hersbach, H. (2010). Comparison of C-band scatterometer CMOD5. N equivalent neutral winds with ECMWF. *Journal of Atmospheric and Oceanic Technology*, 27(4), 721–736. <https://doi.org/10.1175/2009jtecho698.1>
- Hines, C. O., & Reddy, C. (1967). On the propagation of atmospheric gravity waves through regions of wind shear. *Journal of Geophysical Research*, 72(3), 1015–1034. <https://doi.org/10.1029/jz072i003p01015>
- Hines, K. M., Bromwich, D. H., Wang, S.-H., Silber, I., Verlinde, J., & Lubin, D. (2019). Microphysics of summer clouds in central West Antarctica simulated by the Polar Weather Research and Forecasting model (WRF) and the Antarctic Mesoscale Prediction System (AMPS). *Atmospheric Chemistry and Physics*, 19(19), 12431–12454. <https://doi.org/10.5194/acp-19-12431-2019>
- Hong, S.-Y., Lim, K.-S. S., Lee, Y.-H., Ha, J.-C., Kim, H.-W., Ham, S.-J., & Dudhia, J. (2010). Evaluation of the WRF double-moment 6-class microphysics scheme for precipitating convection. *Advances in Meteorology*, 2010, 1–10. <https://doi.org/10.1155/2010/707253>
- Hu, X. M., Klein, P. M., & Xue, M. (2013). Evaluation of the updated YSU planetary boundary layer scheme within WRF for wind resource and air quality assessments. *Journal of Geophysical Research: Atmospheres*, 118(18), 10490–410505. <https://doi.org/10.1002/jgrd.50823>
- Jiménez, P. A., Dudhia, J., González-Rouco, J. F., Navarro, J., Montávez, J. P., & García-Bustamante, E. (2012). A revised scheme for the WRF surface layer formulation. *Monthly Weather Review*, 140(3), 898–918. <https://doi.org/10.1175/mwr-d-11-00056.1>
- Kain, J. S. (2004). The Kain–Fritsch convective parameterization: An update. *Journal of Applied Meteorology*, 43(1), 170–181. [https://doi.org/10.1175/1520-0450\(2004\)043<0170:tkcpau>2.0.co;2](https://doi.org/10.1175/1520-0450(2004)043<0170:tkcpau>2.0.co;2)
- Koch, S. E., Jamison, B. D., Lu, C., Smith, T. L., Tollerud, E. I., Girz, C., et al. (2005). Turbulence and gravity waves within an upper-level front. *Journal of the Atmospheric Sciences*, 62(11), 3885–3908. <https://doi.org/10.1175/jas3574.1>
- Kuester, M., Alexander, M., & Ray, E. (2008). A model study of gravity waves over Hurricane Humberto (2001). *Journal of the Atmospheric Sciences*, 65(10), 3231–3246. <https://doi.org/10.1175/2008jas2372.1>
- Li, X., Clemente-Colón, P., Pichel, W. G., & Friedman, K. (2002). SAR and MODIS images of atmospheric solitary waves generated by upstream blocking in flow over St. Lawrence Island Bering Sea. In *Paper presented at IEEE international geoscience and remote sensing symposium*. IEEE.
- Li, X., Dong, C., Clemente-Colón, P., Pichel, W. G., & Friedman, K. S. (2004). Synthetic aperture radar observation of the sea surface imprints of upstream atmospheric solitons generated by flow impeded by an island. *Journal of Geophysical Research*, 109(C2), C02016. <https://doi.org/10.1029/2003jc002168>
- Li, X., Yang, X., Zheng, W., Zhang, J. A., Pietrafesa, L. J., & Pichel, W. G. (2015). Synergistic use of satellite observations and numerical weather model to study atmospheric occluded fronts. *IEEE Transactions on Geoscience and Remote Sensing*, 53(9), 5269–5279. <https://doi.org/10.1109/tgrs.2015.2420312>
- Li, X., Zheng, W., Yang, X., Li, Z., & Pichel, W. G. (2011). Sea surface imprints of coastal mountain lee waves imaged by synthetic aperture radar. *Journal of Geophysical Research*, 116(C2), C02014. <https://doi.org/10.1029/2010jc006643>
- Li, X., Zheng, W., Yang, X., & Pietrafesa, L. J. (2016). Sea fetch observed by synthetic aperture radar. *IEEE Transactions on Geoscience and Remote Sensing*, 55(1), 272–279. <https://doi.org/10.1109/tgrs.2016.2605670>

- Li, X., Zheng, W., Yang, X., Zhang, J. A., Pichel, W. G., & Li, Z. (2013). Coexistence of atmospheric gravity waves and boundary layer rolls observed by SAR. *Journal of the Atmospheric Sciences*, 70(11), 3448–3459. <https://doi.org/10.1175/jas-d-12-0347.1>
- Lim, K.-S. S., & Hong, S.-Y. (2010). Development of an effective double-moment cloud microphysics scheme with prognostic cloud condensation nuclei (CCN) for weather and climate models. *Monthly Weather Review*, 138(5), 1587–1612. <https://doi.org/10.1175/2009mwr2968.1>
- Lindzen, R., & Tung, K. (1976). Banded convective activity and ducted gravity waves. *Monthly Weather Review*, 104(12), 1602–1617. [https://doi.org/10.1175/1520-0493\(1976\)104<1602:bcaadg>2.0.co;2](https://doi.org/10.1175/1520-0493(1976)104<1602:bcaadg>2.0.co;2)
- Liu, S., Li, Z., Yang, X., Pichel William, G., Yu, Y., Zheng, Q., & Li, X. (2010). Atmospheric frontal gravity waves observed in satellite SAR images of the Bohai Sea and Huanghai Sea. *Acta Oceanologica Sinica*, 29(5), 35–43. <https://doi.org/10.1007/s13131-010-0061-8>
- Mears, C., Lee, T., Ricciardulli, L., Wang, X., & Wentz, F. (2022). RSS Cross-Calibrated Multi-Platform (CCMP) 6-hourly ocean vector wind analysis on 0.25° grid, Version 3.0 [Dataset]. Remote Sensing Systems. <https://doi.org/10.56236/RSS-uv6h30>
- Mendoza, V., Pazos, M., Garduño, R., & Mendoza, B. (2021). Thermodynamics of climate change between cloud cover, atmospheric temperature and humidity. *Scientific Reports*, 11(1), 21244. <https://doi.org/10.1038/s41598-021-00555-5>
- Mesinger, F., & Arakawa, A. (1976). Numerical methods used in atmospheric models.
- MODIS Characterization Support Team (MCST). (2017). MODIS 500m calibrated radiance product [Dataset]. NASA MODIS Adaptive Processing System, Goddard Space Flight Center. <https://doi.org/10.5067/MODIS/MOD02HKM.061>
- Mouche, A. A., Hauser, D., Daloze, J.-F., & Guérin, C. (2005). Dual-polarization measurements at C-band over the ocean: Results from airborne radar observations and comparison with ENVISAT ASAR data. *IEEE Transactions on Geoscience and Remote Sensing*, 43(4), 753–769. <https://doi.org/10.1109/tgrs.2005.843951>
- Mueller, D., Geerts, B., Wang, Z., Deng, M., & Grasmick, C. (2017). Evolution and vertical structure of an undular bore observed on 20 June 2015 during PECAN. *Monthly Weather Review*, 145(9), 3775–3794. <https://doi.org/10.1175/mwr-d-16-0305.1>
- Nappo, C. J. (2013). *An introduction to atmospheric gravity waves*. Academic Press.
- Neale, R. B., Chen, C.-C., Gettelman, A., Lauritzen, P. H., Park, S., Williamson, D. L., et al. (2010). Description of the NCAR community atmosphere model (CAM 5.0). NCAR Technical Note NCAR/TN-486+STR, 1(1), 1–12
- Ollier, S., Watson, S., & Montavon, C. (2018). Atmospheric gravity wave impacts on an offshore wind farm. In *Paper presented at journal of physics: Conference series*. IOP Publishing.
- Powers, J. G., Klemp, J. B., Skamarock, W. C., Davis, C. A., Dudhia, J., Gill, D. O., et al. (2017). The weather research and forecasting model: Overview, system efforts, and future directions. *Bulletin of the American Meteorological Society*, 98(8), 1717–1737. <https://doi.org/10.1175/bams-d-15-00308.1>
- Qing, X., Hui, L., Quanan, Z., Peng, X., Yongcun, C., & Yuguang, L. (2008). Evaluation of ENVISAT ASAR data for sea surface wind retrieval in Hong Kong coastal waters of China. *Acta Oceanologica Sinica*, (4), 57–62.
- Saha, S., Moorthi, S., Pan, H., Wu, X., Wang, J., Nadiga, S., et al. (2010). NCEP Climate Forecast System Reanalysis (CFSR) 6-hourly products, January 1979 to December 2010. [Dataset]. Research Data Archive at the National Center for Atmospheric Research, Computational and Information Systems Laboratory. <https://doi.org/10.5065/D69K487J>
- Skamarock, W. C., Klemp, J. B., Dudhia, J., Gill, D. O., Liu, Z., Berner, J., et al. (2019). *A description of the advanced research WRF model version 4* (Vol. 145). National Center for Atmospheric Research.
- Stoffelen, A., Verspeek, J. A., Vogelzang, J., & Verhoef, A. (2017). The CMOD7 geophysical model function for ASCAT and ERS wind retrievals. *IEEE Journal of Selected Topics in Applied Earth Observations and Remote Sensing*, 10(5), 2123–2134. <https://doi.org/10.1109/jstas.2017.2681806>
- Stull, R. B. (1988). *An introduction to boundary layer meteorology*. Springer Science & Business Media.
- Vachon, P. W., Johannessen, O. M., & Johannessen, J. A. (1994). An ERS 1 synthetic aperture radar image of atmospheric lee waves. *Journal of Geophysical Research*, 99(C11), 22483–22490. <https://doi.org/10.1029/94jc01392>
- Valenzuela, G. R. (1978). Theories for the interaction of electromagnetic and oceanic waves—A review. *Boundary-Layer Meteorology*, 13(1), 61–85. <https://doi.org/10.1007/bf00913863>
- Valkonen, T., Vihma, T., Kirkwood, S., & Johansson, M. M. (2010). Fine-scale model simulation of gravity waves generated by Basen nunatak in Antarctica. *Tellus A: Dynamic Meteorology and Oceanography*, 62(3), 319–332. <https://doi.org/10.3402/tellusa.v62i3.15692>
- Verhoef, A., Portabella, M., Stoffelen, A., & Hersbach, H. (2008). CMOD5\_n—the CMOD5 GMF for neutral winds.
- Xu, Q., Li, X., Bao, S., & Pietrafesa, L. J. (2016). SAR observation and numerical simulation of mountain Lee Waves near Kuril islands forced by an extratropical cyclone. *IEEE Transactions on Geoscience and Remote Sensing*, 54(12), 7157–7165. <https://doi.org/10.1109/tgrs.2016.2596678>
- Zhang, X., Li, X., & Zhang, T. (2020). Characteristics and generations of internal wave in the Sulu Sea inferred from optical satellite images. *Journal of Oceanology and Limnology*, 38(5), 1435–1444. <https://doi.org/10.1007/s00343-020-0046-1>
- Zheng, Q., Shen, S., Yuan, Y., Huang, N., Klemas, V., Yan, X.-H., et al. (2004). Evidence of the coexistence of upstream and downstream solitary wavetrains in the real atmosphere.
- Zheng, Q., Yan, X. H., Klemas, V., Ho, C. R., Kuo, N. J., & Wang, Z. (1998). Coastal lee waves on ERS-1 SAR images. *Journal of Geophysical Research*, 103(C4), 7979–7993. <https://doi.org/10.1029/97jc02176>